A Multi-Scale Dynamical Diagnosis of the South-Central U.S. Flood of March 2016

by

Connor Michael Dacey

A thesis submitted in partial fulfillment of the

requirements for the degree of

Master of Science

Atmospheric and Oceanic Sciences

at the

UNIVERSITY OF WISCONSIN – MADISON

2017

Thesis Declaration and Approval

I, Connor M. Dacey, declare that this thesis titled 'A Multi-Scale Dynamical Diagnosis of the South-Central U.S. Flood of March 2016' and the work presented in it are my own.

Connor M. Dacey	_____	_____
Author	Signature	Date

I hereby approve and recommend for acceptance this work in partial fulfillment of the requirements for the degree of Master of Science:

Jonathan E. Martin	_____	_____
Committee Chair	Signature	Date
Michael Morgan	_____	_____
Faculty Member	Signature	Date
Brett Hoover	_____	_____
Committee Member	Signature	Date

ABSTRACT

In early March 2016, an anomalous upper-tropospheric cyclonic disturbance propagated southeastward from central California to an unusually low latitude over central and southern Mexico. The development of this feature from 08-12 March was instrumental in the production of a high impact synoptic-scale flooding event in which 30-45 cm (12-18 in.) of rain fell in parts of northern Louisiana and far eastern Texas, with some localized areas receiving more than 60 cm (24 in.) of rain. This event, characterized by local National Weather Service offices as a "1-in-500 to 1-in-1000 year" event, resulted in a state of emergency in the southcentral United States. In addition to the heavy rainfall, 7 combined EF0 and EF1 tornadoes and multiple instances of straight-line wind damage and baseball-size hail were reported.

This study first traces the synoptic evolution of the upper trough over the five-day event. Employing a semi-geostrophic frontal circulation diagnostic, it was found that differential tilting across the upper-tropospheric baroclinicity was instrumental in lowering the tropopause over unusually low latitudes. Simultaneously, a developing upper-level jet/front system in the northwesterly flow provided additional development in the region through downward advection of high values of stratospheric potential vorticity. To more quantitatively analyze the change in 500 hPa geopotential heights associated with the upper-level trough, a static quasi-geostrophic potential vorticity (QGPV) inversion diagnostic was utilized. After partitioning the total atmosphere QGPV into a lower (1000-550 hPa) and upper (500-50 hPa) layers, it was found that the upper-level QGPV anomaly accounted for ~ 73% of the total 500 hPa geopotential height perturbations from 08-12 March. Thus, it was

concluded that the upper-level QGPV anomaly exerted the most control on the intensity of the trough.

More than 50% of the total rainfall over the entire five-day event was recorded on 10 March. Accordingly, the analysis focuses on the synoptic and meso-scale forcings that were involved in producing the record-breaking rainfall for portions of central and northern Louisiana on that day. Implementing the same static QGPV inversion to analyze the poleward geostrophic moisture flux (PGMF) convergence over the state of Louisiana, it was found that the upper-level QGPV anomaly again accounted for ~ 60% of the total PGMF. Additionally, the forcing for ascent was proved by 850 hPa frontogenesis located over Louisiana in an environment that was also characterized by convective instability. These factors, combined with enhanced PGMF driven substantially by an upper-tropospheric QGPV anomaly, all collectively produced an environment conducive for record-breaking rainfall and locally severe convection.

ACKNOWLEDGEMENTS

Completing this master's thesis was no doubt the most difficult task I have ever endured. Without the support and guidance from a number of specific individuals, I am sure that I would not have been able to succeed. Therefore, it is important that I address and thank some of the people that motivated and helped me throughout this process.

First, I want to thank my advisor, Dr. Jonathan Martin. Initially, when I was debating where to go to graduate school, I honestly hadn't thought much about the University of Wisconsin-Madison. I knew that I wanted to continue my education in meteorology or atmospheric sciences, but a huge part of me really wanted to jump into convective initiation and mesoscale studies. That all changed when I finally decided to apply to UW-Madison and met Dr. Martin on my site visit. I realized within the first few minutes of talking with him that I wanted to work with him, and that synoptic meteorology was my true research passion. I really enjoyed listening to his enthusiasm and pure love for the weather. He understood my interests in subjects such as homeland security, operational meteorology, and environmental policy, and respected my career aspirations to one day work as an emergency manager and a Certified Consulting Meteorologist (CCM). H promised we would work on a project that would expand my insight into synoptic meteorology while also giving me the skills to prepare me for a career of my liking. He made good on his promise, and before you knew it, I was working on a fascinating case study of an extreme flooding event in the southcentral U.S. I have learned an exponential amount from Dr. Martin over the brief two years I was part of his research group, and for that I will forever be thankful. Thank you Dr. Martin for challenging me and for your continued support (despite my inability to this day correctly

describe the QGPV inversion in synoptic terminology!). Thank you for also encouraging me to follow my aspirations, and supporting me on my next adventure at the University of Delaware where I hope to receive a Ph.D. in Disaster Science and Management.

I also want to extend a huge thank you to Melissa Breeden and Coda Phillips. Melissa, thank you so much for your endless time and patience regarding my endless MATLAB and other programming questions! I could not have completed any type of QGPV inversion analysis without the ability to use and alter the codes and scripts you previously wrote. I realize at times that I may have been quite an annoyance, but believe me when I say I owe a huge chunk of my thesis success to you, and for that I will forever be in your debt! I also thank Coda Phillips for helping me (almost daily for hours on end) with constant MATLAB questions and requests. Anyone that knows me already knows that I despise programming more than any other activity, so without the expert programming experience of Coda, I would most certainty not have been able to complete this thesis in time (if at all!).

I also want to thank Dr. Michael Morgan and Dr. Brett Hoover for their willingness to be on my Master's committee and for the advice and support they have given me throughout this process. I have greatly enjoyed getting to know both of them during my time here at UW-Madison! I also want to thank Pete Pokrandt for all his IT help!

Finally, but not least, I want to thank my friends in the AOS department. I could not have asked for a better group of friends to endure graduate school with over the past 2 years. James Simkins, Skylar Williams, Simran Raju, Elliot Shiben, Sean Ridge, Becky Schultz, and William Hahn, I am extremely thankful to have studied with you during our time at UW-Madison. Thank you also to my family for supporting me throughout this entire experience!

Through all the stress of programming problems and thesis writing, they were always there to listen to me complain! Thanks for all you do for me! Love you!

TABLE OF CONTENTS

ABSTRACT i

ACKNOWLEDGEMENTS iii

TABLE OF CONTENTS vi

LIST OF FIGURES vii

LIST OF TABLES xi

LIST OF EQUATIONS xii

1. INTRODUCTION 1

1.1 Historical Review 9

a. Introduction to Upper Level Fronts 9

b. Along-Jet Geostrophic Temperature Advection 14

c. Upper-Level Fronts and their Impacts on Upper-Level Troughs 16

d. PV Thinking and Inversion 16

1.2 Synoptic Evolution 18

a. 08 March 2016 18

b. 09 March 2016 21

c. 10 March 2016 23

d. 11-12 March 2016 25

2. METHODOLOGY 31

2.1 Data 31

2.2 Sawyer–Eliassen Circulation Equation 32

2.3 The Piecewise Static Quasigeostrophic Potential Vorticity Inversion 36

a. Technique and Definitions 36

b. Mean and Perturbation Fields 37

2.4 QGPV Inversion and Poleward Geostrophic Moisture Flux 39

3. RESULTS 41

3.1 Sawyer–Eliassen Circulation 41

3.2. QGPV Inversion Comparisons 46

a. QGPV Checks 47

b. Partitioned Full QGPV Inversion Geopotential Heights: Mean and Perturbation 49

c. Partitioned TOT_{PERT}: U_{PERT} and L_{PERT} 52

d. 500 hPa Geopotential Height Perturbation Analysis 56

e. 500 hPa Geopotential Height Tendency Analysis 58

3.3. Further analysis of 10 March 2016 including QGPV Inversion 60

3.4. Discussion 71

4. CONCLUSION 72

5. FUTURE WORK 74

REFERENCES 76

LIST OF FIGURES

Figure 1. Rainfall totals greater than 5 cm from 0000 UTC 08 March 2016 to 1800 UTC 12 March 2016. Data provided by the National Weather Services' Advanced Hydrologic Prediction Service. 4

Figure 2. NCEP final analysis of the 500 hPa geopotential heights (black solid) and standardized geopotential height anomalies (shaded) on (a) 0000 UTC 08 March 2016, (b) 0000 UTC 09 March 2016, and (c) 0000 UTC 10 March 2016. 7

Figure 3. Schematic illustration of idealized configurations of potential temperature along a straight jet streak maximum on an upper tropospheric isobaric surface from Lang and Martin (2012) . Geopotential height (thick solid), potential temperature (dashed), isotachs (thin solid filled) with the jet maximum represented by J, and a sense of the mid-tropospheric Sawyer–Eliassen vertical motions (up or down) for: (a) no thermal advection along the jet; (b) geostrophic cold air advection along the jet; and (c) geostrophic warm air advection along the jet. 13

Figure 4. 0000 UTC 08 March 2016 (a) 300 hPa geopotential heights (solid black contour) contoured every 60 m and geostrophic isotachs (shaded) beginning at 30 m s^{-1} in 10 m s^{-1} increments (b) 500 hPa geopotential heights (solid black contour) contoured every 60 m and isentropes (red dashed) every 3 K (c) 850 hPa geopotential heights (solid black contour) contoured every 30 m and isentropes (red dashed) every 3 K (d) Sea-level pressure (solid black contour) contoured every 4 hPa and 950 hPa isentropes (red dashed) contoured every 3 K. 20

Figure 5. 0000 UTC 09 March 2016 (a) 300 hPa geopotential heights (solid black contour) contoured every 60 m and geostrophic isotachs (shaded) beginning at 30 m s^{-1} in 10 m s^{-1} increments (b) 500 hPa geopotential heights (solid black contour) contoured every 60 m and isentropes (red dashed) every 3 K (c) 850 hPa geopotential heights (solid black contour) contoured every 30 m and isentropes (red dashed) every 3 K (d) Sea-level pressure (solid black contour) contoured every 4 hPa and 950 hPa isentropes (red dashed) contoured every 3 K. 22

Figure 6. 0000 UTC 10 March 2016 (a) 300 hPa geopotential heights (solid black contour) contoured every 60 m and geostrophic isotachs (shaded) beginning at 30 m s^{-1} in 10 m s^{-1} increments (b) 500 hPa geopotential heights (solid black contour) contoured every 60 m and isentropes (red dashed) every 3 K (c) 850 hPa geopotential heights (solid black contour) contoured every 30 m and isentropes (red dashed) every 3 K (d) Sea-level pressure (solid black contour) contoured every 4 hPa and 950 hPa isentropes (red dashed) contoured every 3 K. 24

Figure 7. Radar image taken at 01:55 UTC on 10 March 2016. Data provided by UCAR... 26

Figure 8. 0000 UTC 11 March 2016 (a) 300 hPa geopotential heights (solid black contour) contoured every 60 m and geostrophic isotachs (shaded) beginning at 30 m s^{-1} in 10 m s^{-1} increments (b) 500 hPa geopotential heights (solid black contour) contoured every 60 m and isentropes (red dashed) every 3 K (c) 850 hPa geopotential heights (solid black contour) contoured every 30 m and isentropes (red dashed) every 3 K (d) Sea-level pressure (solid black contour) contoured every 4 hPa and 950 hPa isentropes (red dashed) contoured every 3 K. 27

Figure 9. Radar image taken at 24:55 UTC on 10 March 2016. Date provided by UCAR... 28

Figure 10. 0000 UTC 12 March 2016 (a) 300 hPa geopotential heights (solid black contour) contoured every 60 m and geostrophic isotachs (shaded) beginning at 30 m s^{-1} in 10 m s^{-1} increments (b) 500 hPa geopotential heights (solid black contour) contoured every 60 m and isentropes (red dashed) every 3 K (c) 850 hPa geopotential heights (solid black contour) contoured every 60 m and isentropes (red dashed) every 3 K (d) Sea-level pressure (solid black contour) contoured every 4 hPa and 950 hPa isentropes (red dashed) contoured every 3 K. 30

Figure 11. 0000 UTC 08 March 2016. 400 hPa geostrophic cold air temperature advection (shaded) in units of K s^{-1}, geopotential heights (solid) contoured every 60 meters and potential temperature (dashed) contoured every 2 K. Circled is region of geostrophic cold air advection in cyclonic shear. Cross-section between A_1 and A_2 used in Sawyer-Eliassen Solver. 33

Figure 12. Cross-section between A_1 and A_2 on 0000 UTC 08 March 2016. Geostrophic cold air advection (shaded) every 2 K s^{-1}, isentropes (red solid) contoured every 5 hPa, geostrophic isotachs (yellow solid) contoured ever 10 m s^{-1} starting at 30 m s^{-1}, and positive omega values (black contoured) every 1 dPa s^{-1}. 43

Figure 13. Sawyer-Eliassen Circulation solution in plane of cross-section from A_1 to A_2. Potential temperature (red solid) contoured every 5 hPa, geostrophic isotachs (yellow solid) contoured every 10 m s^{-1} starting at 30 m s^{-1}, positive omega (green solid) contoured every 1 dPa s^{-1}, and Sawyer-Eliassen negative streamfunction every 300 m hPa s^{-1} 44

Figure 14. 400 hPa geopotential heights (black solid) contoured every 60 m and 350-450 hPa Layer PV every $1x10^{-6}$ PVU (red shaded). (a) 1200 UTC 07 March 2016 (b) 0000 UTC 08 March 2016 (c) 1200 UTC 08 March 2016 (d) 0000 UTC 09 March 2016 45

Figure 15. The 12-hourly locations of the 500 hPa geopotential height minima from the NCEP final analysis (open circles) compared to those obtained from the inversion of the full QGPV field (filled circles) from 0000 UTC 08-12 March. Magnitude of the analysis (full inversion) 500 hPa geopotential height minima are given by numbers to the right (left) of the dots in units of dm. 48

Figure 16. The 500 hPa geopotential height perturbations associated with the TOT_{pert} QGPV anomaly at (a) 0000 UTC 08 March 2016 (b) 1200 UTC 08 March 2016 (c) 0000 UTC 09 March 2016 (d) 1200 UTC 09 March 2016 (e) 0000 UTC 10 March 2016 (f) 1200 UTC 10 March 2016 (g) 0000 UTC 11 March 2016 (h) 1200 UTC 11 March 2016 (i) 0000 UTC 12 March 2016 (j) 1200 UTC 12 March 2016. The L indicates the position of the 500 hPa full inversion geopotential height minimum for each time step. 50

Figure 17. The 500 hPa geopotential height perturbations associated with the NCEP final analysis at (a) 0000 UTC 08 March 2016 (b) 1200 UTC 08 March 2016 (c) 0000 UTC 09 March 2016 (d) 1200 UTC 09 March 2016 (e) 0000 UTC 10 March 2016 (f) 1200 UTC 10 March 2016 (g) 0000 UTC 11 March 2016 (h) 1200 UTC 11 March 2016 (i) 0000 UTC 12 March 2016 (j) 1200 UTC 12 March 2016 . The L indicates the position of the 500 hPa geopotential height minimum for each time step. 51

Figure 18. The 500 hPa geopotential height perturbations associated with the U_{pert} QGPV anomaly at (a) 0000 UTC 08 March 2016 (b) 1200 UTC 08 March 2016 (c) 0000 UTC 09 March 2016 (d) 1200 UTC 09 March 2016 (e) 0000 UTC 10 March 2016 (f) 1200 UTC 10 March 2016 (g) 0000 UTC 11 March 2016 (h) 1200 UTC 11 March 2016 (i) 0000 UTC 12 March 2016 (j) 1200 UTC 12 March 2016 . The L indicates the position of the 500 hPa full inversion geopotential height minimum for each time step. 53

Figure 19. The 500 hPa geopotential height perturbations associated with the L_{pert} QGPV anomaly at (a) 0000 UTC 08 March 2016 (b) 1200 UTC 08 March 2016 (c) 0000 UTC 09 March 2016 (d) 1200 UTC 09 March 2016 (e) 0000 UTC 10 March 2016 (f) 1200 UTC 10 March 2016 (g) 0000 UTC 11 March 2016 (h) 1200 UTC 11 March 2016 (i) 0000 UTC 12 March 2016 (j) 1200 UTC 12 March 2016 . The L indicates the position of the 500 hPa full inversion geopotential height minimum for each time step. 54

Figure 20. The 6-hour total geopotential height perturbations (TOT_{PERT}) at the location of the fully inverted 500 hPa geopotential height minimum and its two discrete perturbation layers (U_{PERT} and L_{PERT}). The GFS final analysis 500 hPa geopotential height perturbations are also shown. 57

Figure 21. The 6-hourly 500 hPa geopotential height perturbation tendency at the position of the fully inverted 500 hPa geopotential height minimum, computed via a forward difference approximation. 59

Figure 22. Amount of rainfall total that fell on 10 March 2016 as a percentage of the 5-day total. Data provided by the National Weather Service's Advanced Hydrologic Prediction Service..... 61

Figure 23. . 0000 UTC 10 March 2016: (a) 850 hPa PGMF associated with the full atmosphere QGPV inversion (b) 850 hPa PGMF associated with the NCEP final analysis..... 62

Figure 24. 0000 UTC 10 March: 850 hPa PGMF associated with the TOT_{PERT} QGPV anomaly..... 65

Figure 25. 0000 UTC 10 March: (a) 850 hPa PGMF associated with the U_{PERT} QGPV anomaly and (b) PGMF associated with the L_{PERT} QGPV anomaly. 66

Figure 26. 0600 UTC 10 March 2016 850 hPa horizontal frontogenesis (shaded) in units of every 2 K $(1000\ km)^{-1}$ $(3\ hours)^{-1}$ and omega (contoured) every $2x10^{-3}$ Pa s^{-1} with a cross-section along B_1 to B_2..... 68

Figure 27. Cross-section from B_1 to B_2 in Figure 26. Horizontal frontogenesis (red fill) in units of every 2 K $(1000\ km)^{-1}$ $(3\ hours)^{-1}$, omega (blue contoured) every 3 kPa s^{-1}, and potential temperature (green contour) every 3 K..... 69

Figure 28. 0000 UTC 10 March 2016 atmospheric sounding profile of Slidell Muni, LA. Data provided by the University of Wyoming..... 70

LIST OF TABLES

Table 1. Rainfall totals across parts of Texas and Louisiana, beginning on 08 March 2016 and ending at 1400 UTC on 11 March 2016. Data provided by the National Weather Service, Shreveport, LA..... 5

Table 2. 500 hPa geopotential height perturbations (m) associated with the NCEP Final Analyses, and the contribution from TOT_{PERT}, U_{PERT}, and L_{PERT} QGPV anomalies from 0000 UTC 08 March – 1800 UTC 12 March..... 55

LIST OF EQUATIONS

Equation 1. Sawyer (1956) – Eliassen (1962).....32

Equation 2. Rate of Latent Heating…….35

Equation 3. Quasi-Geostrophic Potential Vorticity…….36

Equation 4. Geopotential Field……... 36

Equation 5. Boundary Potential Temperature……..... 36

Equation 6. Quasi-Geostrophic Potential Vorticity Partitions……..... 37

Equation 7. Geopotential Partitions……...…..37

Equation 8. Perturbation Partitions…… 38

Equation 9. Poleward Geostrophic Moisture Flux……..... 40

Equation 10. Mean Poleward Geostrophic Moisture Flux……. 40

Equation 11. Perturbation Poleward Geostrophic Moisture Flux…….....….40

Equation 12. Partitioned Poleward Geostrophic Moisture Flux…….....40

1. INTRODUCTION

Extreme rainfall events have the potential to substantially impact both life and property. In fact, flooding kills more individuals in the United States (U.S.) than any other meteorological phenomenon, and is responsible for 65% of all Presidential Disaster Declarations in the United States[1]. Therefore, it is important for meteorologists to study such events in great detail in order that such research will lead to better understanding of the mechanisms that lead to the extreme rainfall, and to improve forecasts of similar events in the future.

From 08-12 March 2016 the southcentral U.S. was inundated with record-breaking rainfall associated with a potent upper-level low pressure system situated at an unusually low latitude. Throughout this five-day event, the states of Louisiana, Texas, Mississippi, and Arkansas received upwards of 60 cm (2 feet) of rainfall, with the state of Louisiana being hardest hit. Figure 1 shows the spatial extent of the rainfall across Louisiana via quantitative precipitation estimates from the National Weather Services' Advanced Hydrologic Prediction Service[2]. Impressive rainfall totals over the duration of the five-day event at specific locations in Louisiana include the 29.23 cm (11.51 in.) that fell at Shreveport Regional Airport, and the 56.52 cm (22.25 in.) and 30.48 cm (12 in.) that fell at the towns of Swartz and Bush, respectively (not shown). Figure 1 illustrates that most of the state of Louisiana received at least 5 cm (2 in.) of rainfall, with a few exceptions in the far southeastern and southwestern regions of the state. Additional widespread rainfall between 30-45 cm

[1] http://www.floodsafety.noaa.gov/
[2] https://water.weather.gov/ahps/

(~ 12-18 in.) was recorded across the Arkansas, Louisiana, and Mississippi (ArkLaMiss) region, as emphasized by rainfall totals shown in Table 1. The historic amount of rainfall that fell during this time period also caused over 30 rivers and lakes across the southcentral U.S. to reach their moderate and severe flood stages, with many reaching record crests eclipsing prior all-time highs set back in the early 1900s. In fact, the Sabine River along the Texas and Louisiana border topped a historic crest that unofficially dated back to the year 1884[3].

The combination of rainfall and river flooding washed away roadways and bridges, leaving many closed and impassable. It also created dangerous situations for unsuspecting motorists. The Louisiana National Guard was dispatched by the Governor to aid in the rescuing of motorists and individuals trapped in their homes due to the rising flood waters. Many schools and businesses across the southcentral U.S. were also forced to close in the face of the flooding. To put the extent of the rainfall in perspective, Memphis, TN, though not receiving as much rainfall as locations to its south, had only twice in the past 80 years been inundated by such intense rainfall rates. In just a five-day period, the city of Monroe, LA set a record for the wettest month on record and received half of its annual average precipitation. The National Guard was called upon to provide evacuation assistance, security enforcement, rescues by vehicle, boats, and helicopter, and the distribution and supply of food and water for this city and others. The Louisiana Red Cross opened storm shelters across the state in hopes of providing some comfort to those impacted by the floods not experienced in some cities since Hurricane Katrina in 2005. In the end, a Federal Disaster Declaration was approved for many Louisiana cities, including Bienville, Bossier, Caddo,

[3] https://weather.com/storms/severe/news/historic-south-flooding-march-2016

Caldwell, Claiborne, De Soto, Grant, Jackson, La Salle, Lincoln, Natchitoches, Ouachita, Red River, Sabine, Union, Webster, and Winn Parishes[4].

The southcentral U.S. was also impacted by severe weather during this time period. A weakly stratified environment over eastern portions of Texas from 08-09 March 2016 resulted in the development of tornadoes and mesocyclones associated with a mesoscale convective system (MCS). Officially, the local National Weather Service offices confirmed seven weak tornadoes[5]. Fortunately, no fatalities were reported as direct results of these tornadoes, but they still caused damage to cars, local homes, and businesses. Strong winds in excess of 32 m s^{-1} (70 mph) associated with severe convection and a squall line that moved through the Dallas-Forth Worth region also caused straight-line wind damage and left over 400,000 Dallas-area customers without power. Hail also posed a major threat, with golfball-sized hail reported in the cities of Evant, TX and Jonesboro,TX, and hail the size of baseballs reported in the city of Voca, TX.

This medley of sensible weather had large impacts across the south-central U.S., specifically across the states of Texas and Louisiana. This event caused approximately $350 million in property damage and was directly responsible for the deaths of four individuals. The flooding was historic, prompting the Louisiana Emergency Management community to suggest it was unprecedented and the National Weather Service offices to refer to it as a "1-in-500" to "1-in-1000" year event.

One of the most notable aspects of this case was the development and propagation of an upper-level trough from 08-12 March 2016 that, originally off the southern coast of

[4] https://www.ncdc.noaa.gov/stormevents/
[5] http://www.spc.noaa.gov/archive/

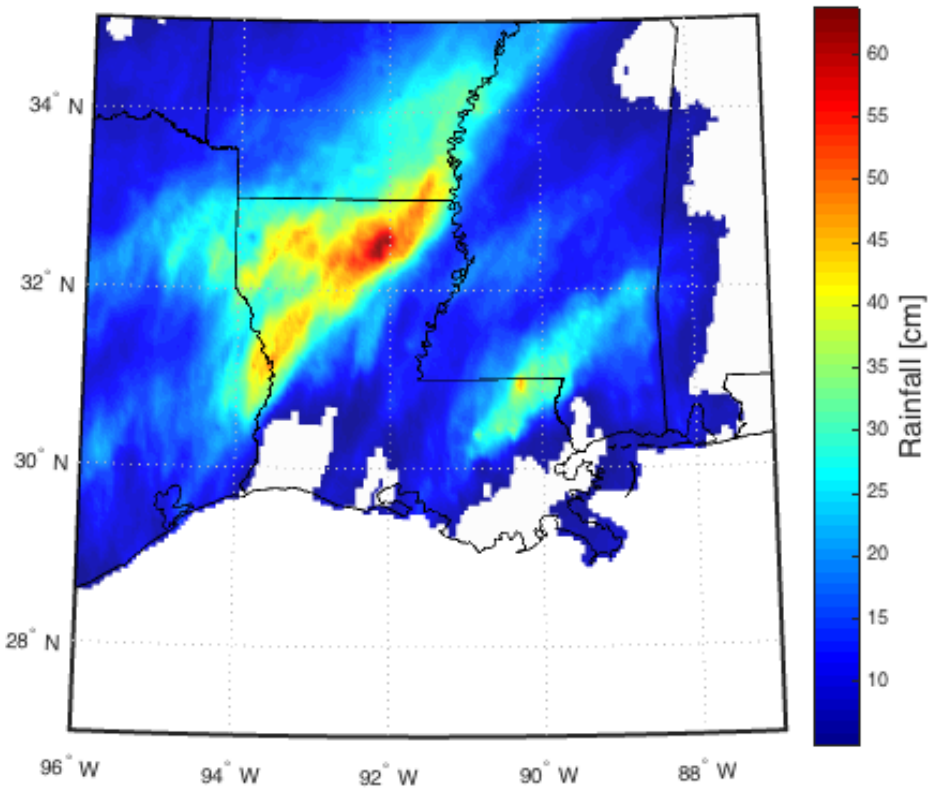

Figure 1. Rainfall totals greater than 5 cm from 0000 UTC 08 March 2016 to 1800 UTC 12 March 2016. Data provided by the National Weather Services' Advanced Hydrologic Prediction Service.

Location	Rainfall Total (cm)	Rainfall Total (inches)
Taylortown, Bossier Parish, LA	46.71	18.39
Red River Research Station, Bossier City, Bossier Parish, LA	42.67	16.80
Barksdale AFB, Bossier Parish, LA	47.85	18.84
Jamestown, Bienville Parish, LA	39.93	15.72
Koran, Bossier Parish, LA	38.99	15.35
Center, Shelby County, TX	26.47	10.42
Homer, Claiborne Parish, LA	37.24	14.66
Minden, Webster Parish, LA	45.80	18.03
Arcadia, Bienville Parish, LA	38.61	15.20
Swartz, Ouachita Parish, LA	56.52	22.25
Longview, Gregg County, TX	23.11	9.10
Tyler, Smith County, TX	18.59	7.32
Monroe, Ouachita Parish, LA	51.46	20.26
Colombia Lock, Colombia, Caldwell Parish, LA	22.68	8.93
Southern Hills, Shreveport, Caddo Parish, LA	33.38	13.14
Natchitoches, Natchitoches Parish, LA	41.76	16.44
Marshall, Harrison County, TX	27.33	10.76
Carthage, Panola County, TX	28.27	11.13
Shreveport Regional Airport, Caddo Parish, LA	29.24	11.51

Table 1. Rainfall totals across parts of Texas and Louisiana, beginning on 08 March 2016 and ending at 1400 UTC on 11 March 2016. Data provided by the National Weather Service, Shreveport, LA.

California, gained increasingly anomalous classification as it migrated to an unusually southern latitude and became centered over southwest Mexico on 10 March 2016. It was this trough that provided the ideal environmental conditions necessary for the excessive flooding that was observed, as its associated low- and mid-level circulations funneled tropical moisture into parts of the southern U.S. and Mississippi Valley regions. What is unique about this trough is its anomalous behavior over this five-day period. Figure 2 depicts the 500 hPa geopotential heights and standardized anomalies for the first three days of the event. At 0000 UTC 08 March (Fig. 2a), the upper-level trough was located over southern California, with standardized anomalies around two-sigma below the 31-year (1979-2010) climatological mean. Just 24 hours later at 0000 UTC 09 March (Fig. 2b), the upper-level circulation had intensified and became more isotropic. Given its rapid southeastward propagation, the standardized anomalies by this time were maximized at more than six standard deviations (six-sigma) below the climatological mean. By the time it had reached its lowest latitude at 0000 UTC 10 March (Fig. 2c), the upper-level low was characterized as a 12-sigma event, emphasizing the extremely anomalous nature of this trough, a combination of its intensity and its unusual southern latitude in mid-March.

This study investigates the development and evolution of the anomalous upper-tropospheric trough that characterized this event from 08 – 12 March 2016, while also investigating the mechanisms that produced the flooding in the southcentral U.S. One of the most notable aspects of this event was the coincident development of an upper-tropospheric frontal structure while in northwesterly flow attendant with the southerly propagation of the

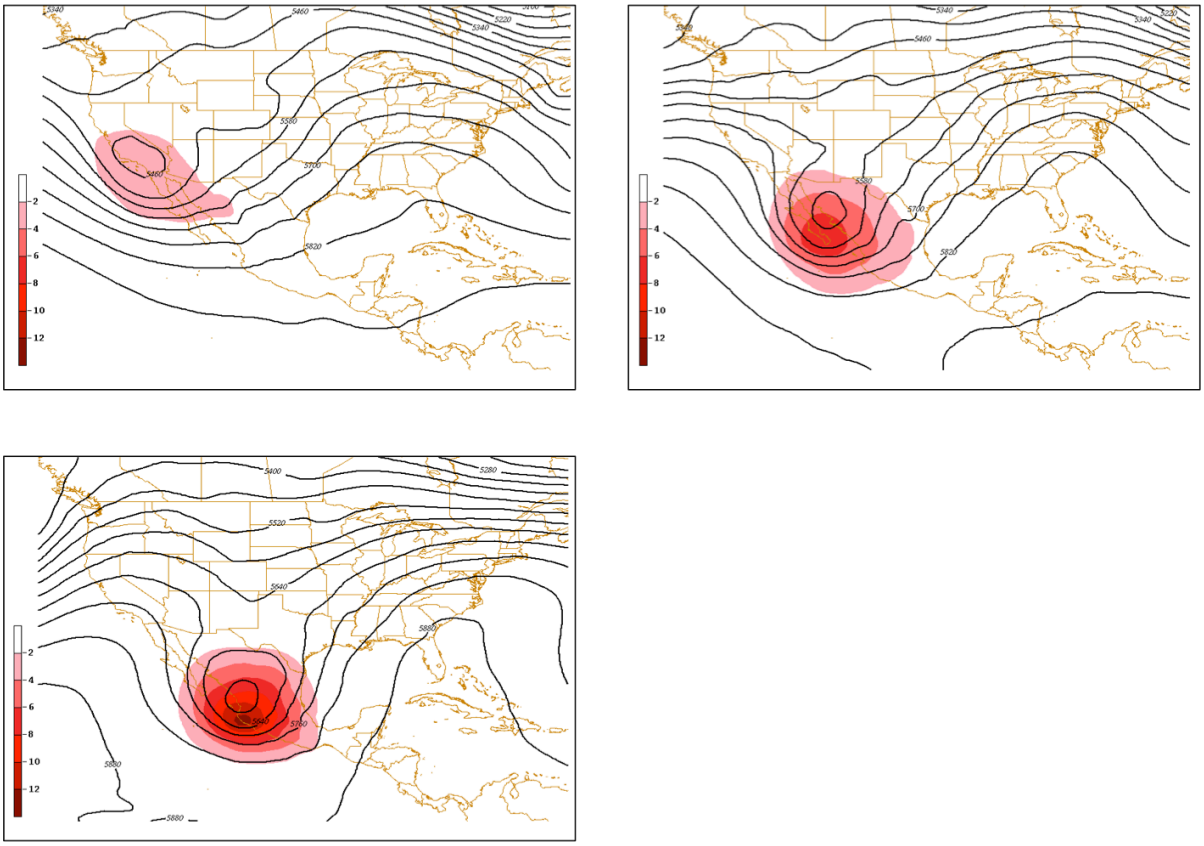

Figure 2. NCEP final analysis of the 500 hPa geopotential heights (black solid) and standardized geopotential height anomalies (shaded) on (a) 0000 UTC 08 March 2016, (b) 0000 UTC 09 March 2016, and (c) 0000 UTC 10 March 2016.

500 hPa trough. Though the development of upper-level fronts is not uncommon, previous studies have shown that they can play an important role in the development of high-impact precipitation events (e.g. Uccellni et al., 1985; Whitaker et al. 1988 Lackmann et al. 1997; Winters and Martin 2014) and conspire to produce heavy flooding events in an unusual synoptic way – i.e. the primary flood area is located downstream of the upper-level trough. Thus, an investigation into upper-tropospheric frontal structures and their impacts on upper-level troughs must be employed to gain insight into the physical processes that were involved in creating this high-impact weather event.

The following chapter will present a historical literature review focusing on the development of upper-level fronts and their influence on upper-level troughs, and subsection 1.2 will focus specifically on the synoptic evolution of the March 2016 trough. Chapter 2 will then focus on the utilization of the Sawyer–Eliassen circulation diagnostic to investigate the development of an upper-tropospheric front. To more quantitatively study the evolution of this trough, a QGPV inversion technique, similar to that employed by Martin and Marsili (2002) using Ertel PV will also be discussed and employed in Chapter 2. The results of these diagnostics will be presented in Chapter 3, and will address the synoptic evolution of the upper-level trough that helped set in motion the sequence of events that resulted in the extreme flooding. After investigating the propagation of the upper-level trough to the southeast, this study also aims to use the same QGPV inversion process to study the poleward geostrophic moisture flux (PGMF) over the state of Louisiana on 10 March, the day on which parts of northern Louisiana received more than 50% of the total rainfall associated with the entire event. These results are presented at the end of Chapter 3. Final

conclusions regarding the March 2016 flooding event and suggestions for future analysis can be found in Chapters 4 and 5, respectively.

1.1 Historical Review

a. Introduction to Upper Level Fronts

Upper level jet-front systems are characterized by a local wind speed maximum and a large horizontal temperature gradient along a sloping midlatitude tropopause surface (Lang and Martin 2012). The development of upper tropospheric fronts and their effects on upper-level troughs have been topics of active research since the early to mid-1950s. At the start of the decade, Reed and Sanders (1953) examined a case of intense 500 hPa frontogenesis, treating the thermal and vorticity aspects of frontogenesis separately, and found via radiosonde data that certain regions of the frontal zone were of stratospheric origin. A peculiar characteristic of these features was the apparent cross-shear gradient in subsidence, with the strongest subsidence at the warm edge of this baroclinic zone. Such differential subsidence was then responsible for frontogenetic tilting of isentropes. Further investigation led to employment of potential vorticity (PV) on isentropic surfaces to study the formation of upper-level frontal zones (Reed 1955). In that study, Reed concluded that despite the fact that these frontal zones acquired temperature characteristics associated with tropical air, the zones actually formed completely in the polar air mass. It was believed that this was due to the strong subsidence located near the warm boundary, which simultaneously provided the means by which the thermal contrast was intensified, the tropopause became folded into a characteristic "S" shape and, some amount of stratospheric air was subducted into the middle and upper troposphere. This represented one of the first studies to highlight tilting

frontogenesis, in which the ageostrophic circulations associated with jet streaks could promote upper-level frontogenesis by intensifying the isentropic gradient via differential tilting in the vertical. Soon after, the subduction of stratospheric air into the upper troposphere via the formation of upper level fronts became the topic of numerous studies relating to stratosphere-troposphere exchange (e.g. Danielsen 1964; Shapiro 1980; Stohl et al. 2003).

Following the work by Reed (1955), Reed and Danielsen (1959) used measurements of radioactivity to demonstrate that these upper tropospheric fronts contained air that originated in the lower stratosphere. Understanding exchange processes between the troposphere and stratosphere became increasingly important at this time due to concerns that radioactivity released from nuclear weapons testing in the stratosphere could reach the surface and lead to health issues. They found that measurements of the radioactive fallout in the upper troposphere proved consistent with the tilting frontogenesis theory. This study also emphasized the ability for upper-tropospheric fronts to subduct atmospheric constituents (such as nuclear debris) located in the lower stratosphere into the middle and upper troposphere. Once in the troposphere, the radiation could then be turbulently mixed throughout the atmosphere and possibly negatively impact human health at the surface. Thus, research on upper-level fronts and their effects became essential to understanding stratospheric-tropospheric exchange for both meteorological and human-health reasons. As Lang and Martin (2012) mentions, their conceptual model is consistent with the tilting frontogenesis theory that slowly gained more acceptance through the early 1960s after

aircraft measurements of tracers such as water vapor, ozone, and radioactivity independently confirmed stratospheric air within these tropopause folds (Keyser and Shapiro 1986).

At about the same time, investigations into frontal circulations began to emerge. In his 1956 paper, Sawyer investigated the relationship between vertical circulations at fronts and the overall process of frontogenesis. The main goal of his research was to explore the suggestion that fronts are areas into which active confluence of air currents of different temperature are taking place. Using air parcel trajectories and temperature observations, Sawyer was able to support this claim by noting that in many cases, the existence of such confluence was undeniable, and that cooling occurred often on the warm side of the frontal zone and conversely, warming occurred on the cold side. In fact, Sawyer found that 13 of the 20 fronts examined in his study supported the declaration that frontogenesis leads to a vertical circulation which causes ascent of the warm air and descent of the cold air and the formation of an inclined frontal zone. To quantitatively describe the vertical and cross-isobar flow, Sawyer investigated a simplified model that assumed (1) the horizontal flow would concentrate the temperature gradient near the central stream-line and (2) the flow has the same general form at all levels, but in accordance with geostrophic balance, the velocity in the direction of the isotherms increases with height. His mathematical expression was examined for six different frontal zones. Overall, Sawyer (1956) was the first to derive a one-dimensional version of what is now known as the Sawyer (1956)–Eliassen (1962) equation by showing how the resulting vertical circulations in relation to fronts can be calculated. His study was then expanded upon by Eliassen (1962) who focused on the transverse circulations set up in response to variations in wind and temperature along the frontal zone, and provided

a two-dimensional theory for the cross-front and vertical ageostrophic transverse circulations. The resulting Sawyer (1956) – Eliassen (1962) equation connected the primary geostrophic frontogenetic forcing with the creation of a secondary ageostrophic circulation around a frontal zone. Eliassen explained that the frontogenesis process worked in two steps. First, the geostrophic deformation forces intensification of the temperature gradient. Second, in response to thermal wind imbalance, secondary ageostrophic circulations develop which act to further strengthen the temperature gradient.

Further investigation into the ageostrophic transverse circulations associated with idealized variations of the upper-tropospheric geostrophic shearing and stretching deformation forcing terms in the Sawyer (1956) – Eliassen (1962) equation continued in a study by Shapiro (1982). He found that, in the absence of along-jet geostrophic temperature advection, the Sawyer–Eliassen circulation was manifest in the traditional four-quadrant model with a thermally direct (indirect) circulation in the jet entrance (exit) region (Fig. 3a). However, in locations where there was geostrophic cold air advection across the jet core, the thermally direct (indirect) circulation in the jet entrance region was "shifted" to the anticyclonic (cyclonic) side of the jet so that the subsidence is present through the jet maximum, as shown in Fig. 3b. This shifting of the subsidence is upper-frontogenetic. Conversely, geostrophic warm air advection along the jet core results in a "shift" of the thermally direct (indirect) circulation in the jet entrance (exit) region toward the cyclonic (anticyclonic) side of the jet. This then results in ascent through the jet maximum, as represented in Fig. 3c.

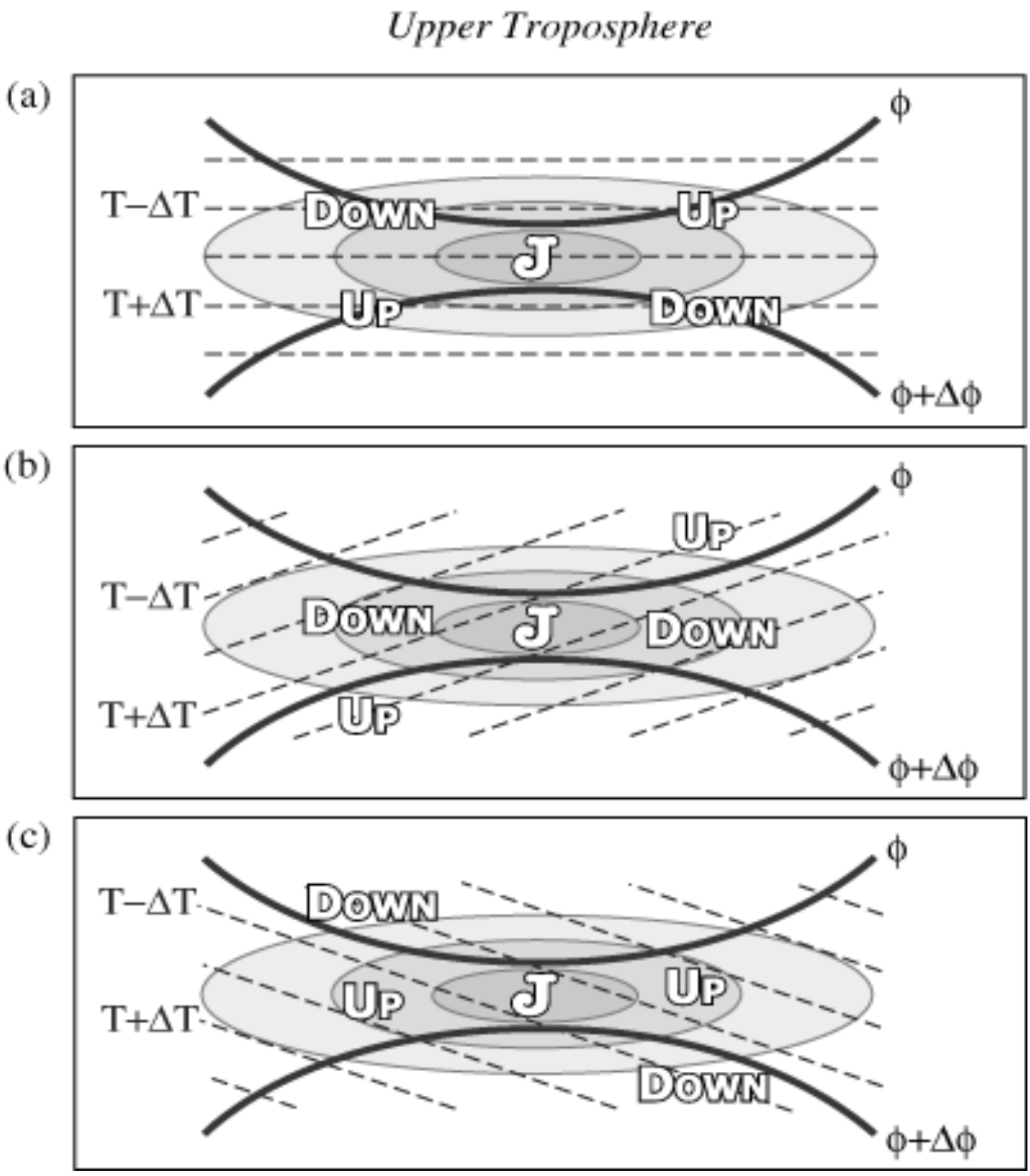

Figure 3. Schematic illustration of idealized configurations of potential temperature along a straight jet streak maximum on an upper tropospheric isobaric surface from Lang and Martin (2012) . Geopotential height (thick solid), potential temperature (dashed), isotachs (thin solid filled) with the jet maximum represented by J, and a sense of the mid-tropospheric Sawyer–Eliassen vertical motions (up or down) for: (a) no thermal advection along the jet; (b) geostrophic cold air advection along the jet; and (c) geostrophic warm air advection along the jet.

b. Along-Jet Geostrophic Temperature Advection

Many studies have since concluded that an environment characterized by geostrophic cold air advection through the jet core is an important characteristic of upper-tropospheric frontal development, as the resulting vertical motions have been shown to have frontogenetic effects in the upper troposphere (Schultz and Doswell 1999; Lang and Martin 2012; Martin 2014). Keyser and Pecnick (1985) utilized a two-dimensional primitive equation model to investigate the effect of confluence and horizontal shear on the development of upper-tropospheric fronts. They note that observational evidence has shown that upper-level frontogenesis and tropopause folding are favored in a northwesterly flow regime upstream of a "digging" diffluent trough within an amplifying baroclinic wave. Due to the thermal wave lagging the height wave, geostrophic cold air advection occurs along the frontal zone and provides the possibility of upper-level frontogenesis. Their modeling results showed that for a case of geostrophic cold air advection in cyclonic shear, the upper-level frontogenesis that developed looked extremely similar to that identified in the 1950s and 1970s using radiosonde and aircraft data, respectively. Consistent with Shapiro's hypothesis, they also found the cross-front ageostrophic circulations were thermally direct, but shifted towards the warm air so that the subsidence is maximized directly underneath the jet core. Their results also help clarify a unique aspect of cross-front ageostrophic circulations associated with upper-level frontogenesis: A thermally indirect circulation is needed for tilting frontogenesis, while a thermally direct circulation is needed to maintain or increase the kinetic energy of the upper-level jet. Though seemingly paradoxical, the shift of the subsidence maximum to the warm side of the developing front in cases of geostrophic cold

air advection in northwesterly flow results in a vertical motion pattern that appears to be indirect locally, but direct when viewed from a larger perspective.

While many previous studies have focused on upper frontogenetic tilting forced by transverse circulations that are a result of frontogenesis associated with confluence and horizontal shear, recent work by Martin (2014) asserts that although these studies have greatly contributed to the overall understanding of the upper frontogenesis process, there has been a lack of emphasis on the role of differential vorticity advection in this same process as first outlined by Mudrick (1974) in an idealized simulation of upper frontogenesis. To elaborate, Martin (2014), while analyzing two cases of upper frontogenesis in northwesterly flow, demonstrated that the predominant sinking motion that drives upper frontogenesis can be related to negative geostrophic shear vorticity advection by the thermal wind. In fact, regions of geostrophic cold air advection in cyclonic shear are *always* characterized by negative geostrophic vorticity advection by the thermal wind. He found that in geostrophic cold air advection cases, the subsidence associated with the geostrophic shear vorticity advection by the thermal wind is always distributed in a narrow, quasi-linear frontal-scale column beneath the jet core along the warm edge of the upper baroclinic zone, similar to the results of past studies. In fact, Martin (2014) claims that "Mudrick's (1974) emphasis on negative vorticity advection increasing with height combined with Shapiro's (1981) insight regarding the lateral displacement of frontogenetic transverse circulations is the most comprehensive way to conceptualize the forcings that promote rapid upper level jet-front development in regions of geostrophic cold air advection in cyclonic shear." Importantly, his results also emphasized that the subsidence associated with vorticity advection by the thermal

wind is not of the transverse variety, but rather shearwise- a distinction that may be important when considering the energetics of upper frontogenesis.

c. Upper-Level Fronts and their Impacts on Upper-Level Troughs

The development of upper-level fronts can also impact the evolution of upper-tropospheric troughs (Sanders et al. 1990; Schultz and Sanders 2002). The subduction of high PV stratospheric air into the middle and upper troposphere can lead to environments characterized by anomalously large PV whose downstream leading edges can be charactertized by positive PV advection, which serves to lower the geopotential heights and intensify the circulation. In cases of upper-level frontal development in northwesterly flow, the PV advection lowers heights to the southeast and can drive troughs to lower latitudes. Though the Sawyer–Eliassen circulations give information about the deformation of the tropopause and the downward protrusion of high PV into the upper troposphere, the resulting height changes are better diagnosed using some form of potential vorticity (PV) inversion.

d. PV Thinking and Inversion

PV is one of the most useful diagnostic tools in the synopticians' arsenal as a consequence of its ability to effectively describe both the dynamic and thermodynamic properties of the atmosphere at all scales (Posselt 2004). The concept of "PV thinking" is credited to Hoskins et al. (1985), who demonstrated the usefulness of PV as a tool to examine mid-latitude weather systems. They explained that while assuming both adiabatic and inviscid flow, PV serves an adequate tracer for atmospheric motion. They also noted that the mass, momentum, and thermal fields associated with a specific PV distribution could, under suitable analytic conditions, be recovered through the process of *inversion*. Kleinschmidt

(1957) is credited as being the first to perform a PV inversion, however it was not until Hoskins et al. (1985) introduced more specific theoretical groundwork for PV inversion that the usefulness of PV as a diagnostic tool began to be recognized (Posselt 2004). To expand on this idea, Hoskins et al. (1985) mention that the full PV field can essentially be divided into an infinite number of pieces, each of which are associated with specific mass and thermal perturbation fields (Hakim et al. 1996). For example, a positive (negative) PV anomaly is associated with a cyclonic (anticyclonic) circulation that is greatest in magnitude at the same level as the anomaly and decays with altitude both above and below the anomaly (Martin 2006). Associated with this development of a positive (negative) PV anomaly is the associated cold (warm) column of air below the anomaly, and warm (cold) column of air above it (Martin 2006).

Davis and Emanuel (1991) expanded upon the work by Hoskins et al. (1985) by developing a numerical piecewise PV inversion technique to examine the influence of discreet portions of the full Ertel PV field on height changes (Korner and Martin 2000; Martin and Marsili 2002; Martin and Otkin 2004). A simpler yet insightful diagnostic tool available for the same purpose, known as static piecewise tendency diagnosis, was initially developed by Hakim et al. (1996) and then further described by Nielsen-Gammon and Lefevre (1996) and uses the full QGPV instead of the full Ertel PV to perform an inversion. Exploiting the fact that the quasi-geostrophic height tendency equation is a statement of conservation of QGPV along a geostrophic trajectory, this technique inverts the Eulerian tendency of QGPV to gain insight into the physical processes that influence height changes. This goal of this technique is to serve as a quantification of the "PV thinking" initially

described by Hoskins et al. (1985). To further present an overview of the five-day evolution of the upper-level trough, the static piecewise QGPV inversion will be utilized and further described in the methodology section.

1.2 Synoptic Evolution

The March 2016 upper-level trough that developed over southern California before propagating to the southeast over central and southern Mexico proved responsible for some of the greatest rainfall totals seen in the southcentral U.S. in recent times. The following section will focus on the evolution of this trough from 08-12 March, providing an analysis of the environmental conditions that were present at the time of this historic event.

a. 08 March 2016

At 0000 UTC 08 March 2016, a tropopause-level jet oriented in a northwest to southeast direction was located off the west coast of the U.S. and Mexico, with an impressive 100 m s^{-1} jet streak at 300 hPa located off Mexico's Baja California (Fig. 4a). At this time, the 500 hPa geopotential height minimum of 5460 m was centered over far southwestern California and located in a region of geostrophic cold air advection (Fig. 4b). The trough was also associated with an impressive meridional temperature gradient located off the coast of western Mexico at 500 hPa, indicative of the presence of a strong upper-tropospheric baroclinic zone. The feature was located between two developing anticyclones, with ridging occurring over the eastern portion of the Gulf of Mexico through parts of the southeastern U.S. and the other building upstream of the trough axis in the subtropical eastern Pacific.

At both 850 hPa (Fig. 4c) and the surface (Fig. 4d), similar synoptic features can also be seen, with anticyclonic regions located both up- and downstream of the upper-level

trough axis. Across the U.S. southern Plains, confluent south-southwesterly flow prevailed at both the upper and lower levels, with low-level (850 hPa) warm air advection occurring into the states of Texas and Louisiana. There is little indication of low-level development at both 850 hPa and at sea-level (Fig. 4d) at this time.

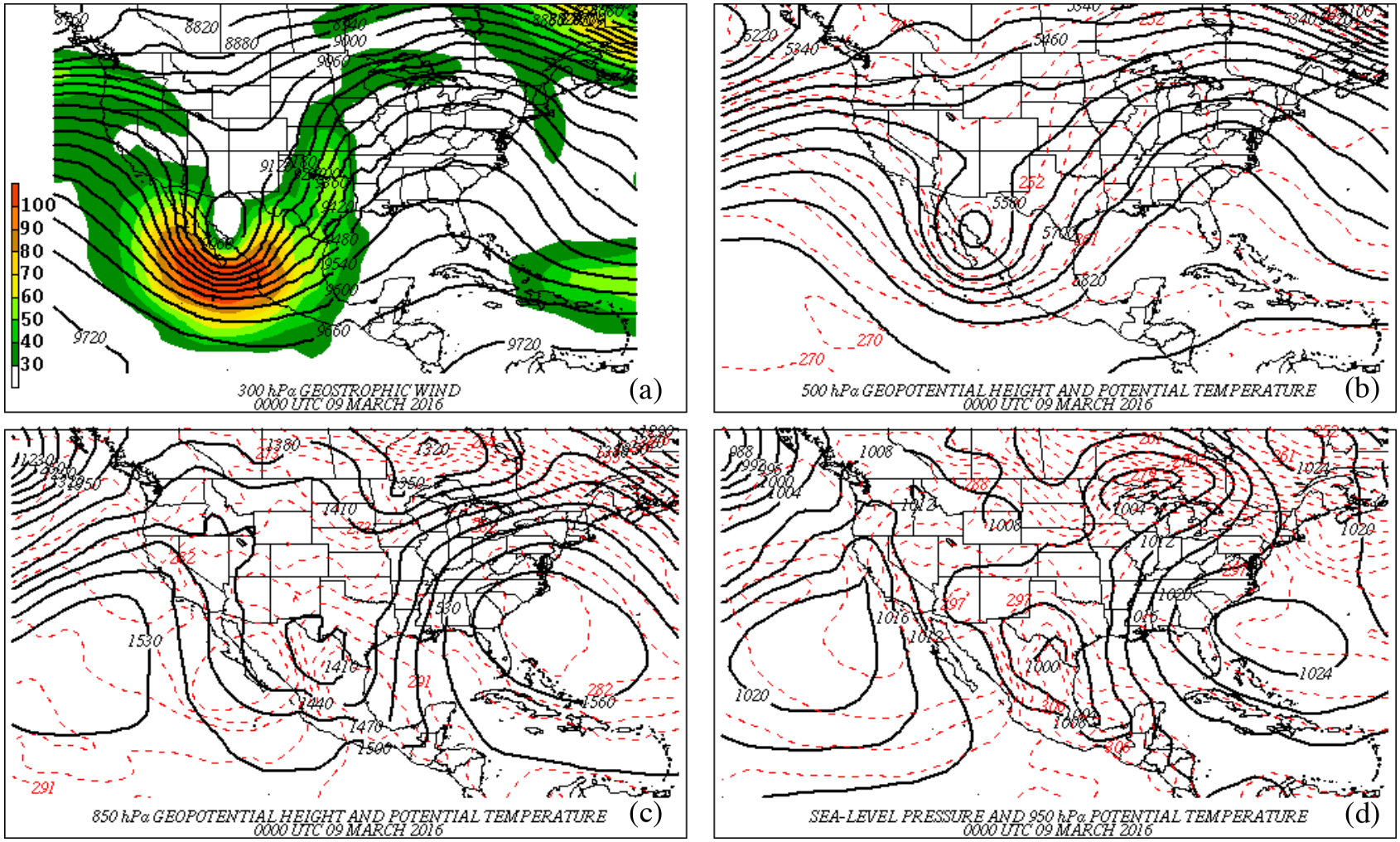

Figure 4. 0000 UTC 08 March 2016 (a) 300 hPa geopotential heights (solid black contour) contoured every 60 m and geostrophic isotachs (shaded) beginning at 30 m s^{-1} in 10 m s^{-1} increments (b) 500 hPa geopotential heights (solid black contour) contoured every 60 m and isentropes (red dashed) every 3 K (c) 850 hPa geopotential heights (solid black contour) contoured every 30 m and isentropes (red dashed) every 3 K (d) Sea-level pressure (solid black contour) contoured every 4 hPa and 950 hPa isentropes (red dashed) contoured every 3 K.

b. 09 March 2016

By 0000 UTC 09 March 2016, the jet streak was located at the base of the upper-level trough, with winds maximized at ~110 m s^{-1} at 300 hPa (Fig. 5a). At 500 hPa, the upper level low was now located over northwestern Mexico with a closed 5520 m geopotential height contour as seen in Fig. 5b, with continuing south-southwesterly flow located over Texas. At 850 hPa, a broad region of low geopotential heights formed over western Texas and north-central Mexico, with low-level warm air advection occurring over the southcentral U.S. An increase of about 5-10 m s^{-1} in the meridional flow since the previous 0000 UTC analysis at 850 hPa over the western Gulf of Mexico (as indicated by the more north-south oriented geopotential height contours in Fig. 5c) advected large amounts of low-level moisture into parts of Arkansas, Louisiana, and Texas that yielded heavy rain across these states. At the surface, a 999 hPa low pressure center also formed at this time over the Texas-Mexico border, southwest of San Antonio, TX (Fig. 5d). The combination of low-level warm air advection and surface dew points across the region that were generally in the upper teens to near 20°C aided in the development of thunderstorms. Sounding profiles across the region at this same time also showed moderate instability with surface convective available potential energy (CAPE) values around 1000 J kg^{-1} and strengthening deep-layer shear profiles of 25-28 m s^{-1}, supporting the development of severe mesocyclones and tornadoes. A mesoscale convective system (MCS) then formed overnight, aided by a strengthening 20-30 m s^{-1} low-level jet (not shown). This MCS tracked eastward as the upper-level low continued to dive southward into central Mexico.

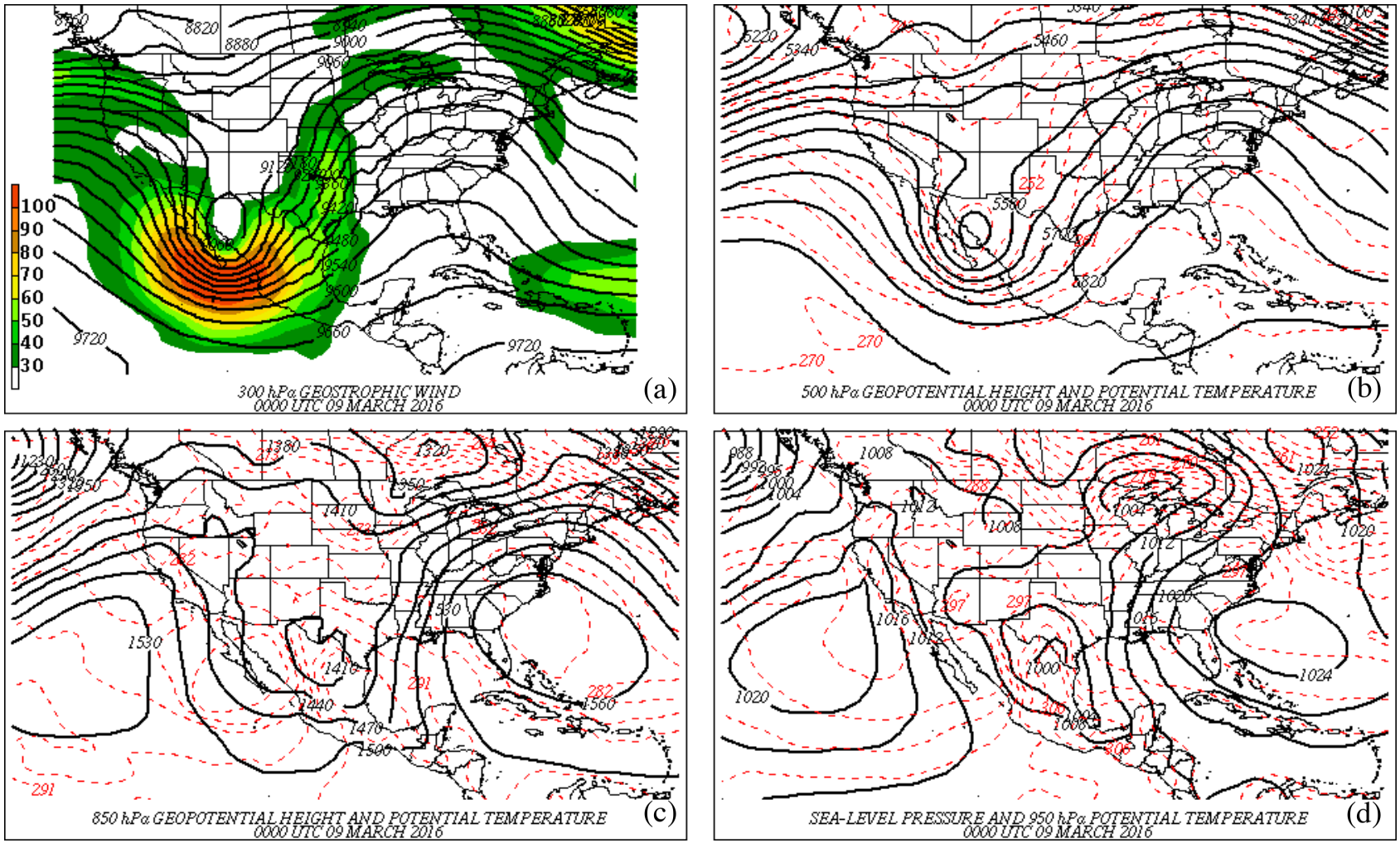

Figure 5. 0000 UTC 09 March 2016 (a) 300 hPa geopotential heights (solid black contour) contoured every 60 m and geostrophic isotachs (shaded) beginning at 30 m s^{-1} in 10 m s^{-1} increments (b) 500 hPa geopotential heights (solid black contour) contoured every 60 m and isentropes (red dashed) every 3 K (c) 850 hPa geopotential heights (solid black contour) contoured every 30 m and isentropes (red dashed) every 3 K (d) Sea-level pressure (solid black contour) contoured every 4 hPa and 950 hPa isentropes (red dashed) contoured every 3 K.

c. 10 March 2016

At 0000 UTC 10 March 2016, the jet streak at 300 hPa continued to round the base of the trough located over southern Mexico (Fig. 6a). The trough axis of the upper-level low at 500 hPa reached its farthest southern position, centered about 37° N latitude over western Mexico (Fig. 6b). Both the 5580 m and 5640 m geopotential height contours became completely cut off from the main flow at this time coincident with a 306 K minimum thermal trough. The 500 hPa ridging associated with the surrounding anticyclones also intensified. The positively tilted ridge axis located upstream of the trough axis continued to build through the eastern Pacific into southern California. The other ridge located downstream of the trough axis also moved northward through Florida and the far southeastern states. These anticyclones are also seen at the lower levels (Fig. 6c, d). At the surface, a 1024 hPa high pressure system is located east of Florida into the western portions of the Atlantic Ocean, and a 1020 hPa high pressure system is located near Hawaii in the eastern Pacific Ocean (Fig. 6d). Figure 6c shows the 850 hPa geopotential height minimum at the time is located along the east coast of Mexico and the Gulf of Mexico. Also noticeable is the fact that the low-level geopotential height contours were oriented in an increasingly north-south orientation that aided in the advection of low-level moisture into the region. Interestingly, the lower tropospheric cyclone's surface low pressure center became more disorganized during this period and weakened slightly to a minimum central pressure of 1001 hPa. However, unlike in previous days, a westward tilt with height associated with this cyclone is noticeable between the 500 hPa and 850 hPa layers, emphasizing the possibility of future strengthening

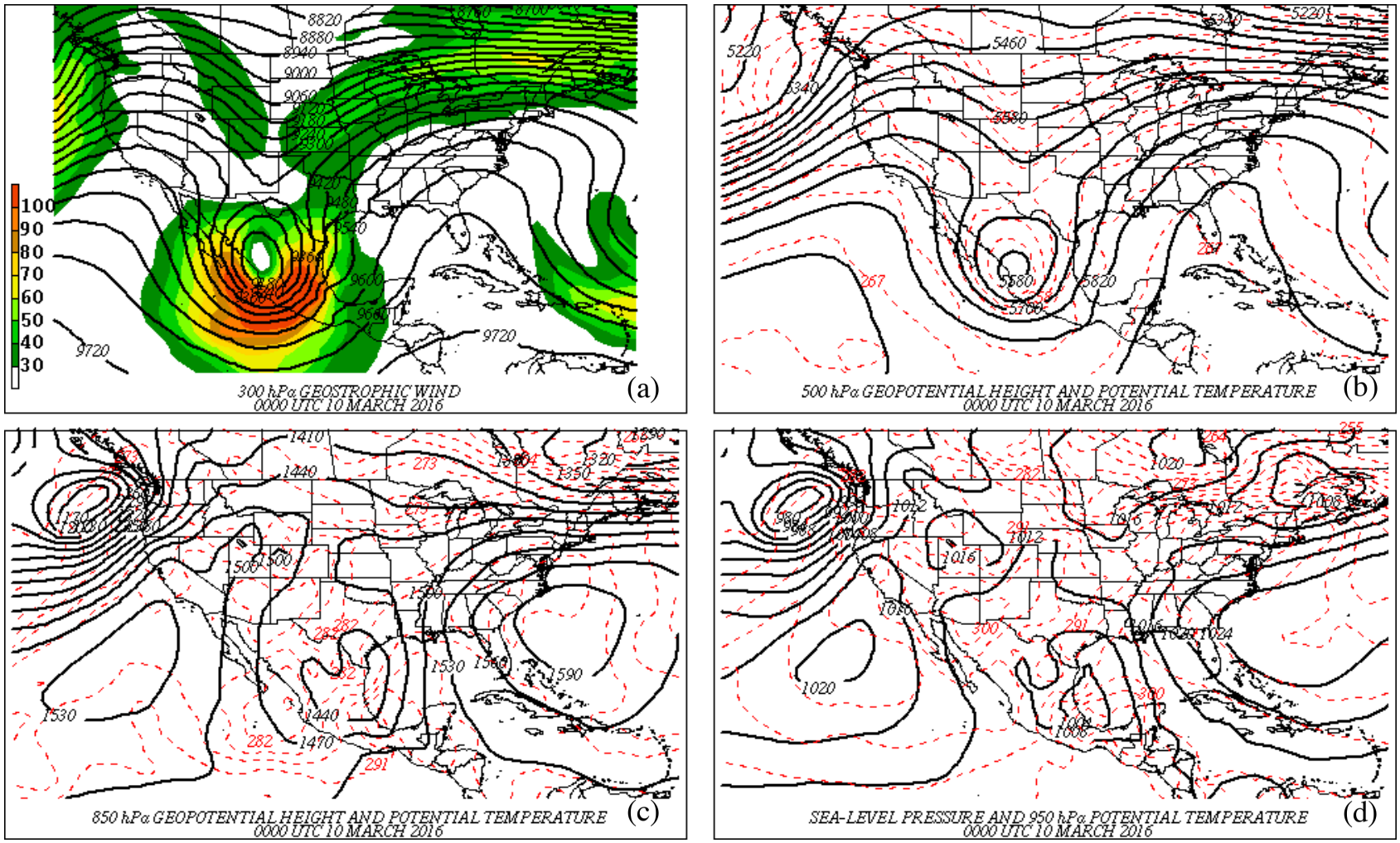

Figure 6. 0000 UTC 10 March 2016 (a) 300 hPa geopotential heights (solid black contour) contoured every 60 m and geostrophic isotachs (shaded) beginning at 30 m s^{-1} in 10 m s^{-1} increments (b) 500 hPa geopotential heights (solid black contour) contoured every 60 m and isentropes (red dashed) every 3 K (c) 850 hPa geopotential heights (solid black contour) contoured every 30 m and isentropes (red dashed) every 3 K (d) Sea-level pressure (solid black contour) contoured every 4 hPa and 950 hPa isentropes (red dashed) contoured every 3 K.

of this cyclone. The threat for severe weather continued, with dew points still hovering in the mid-teens across Texas and Louisiana and 0-6 km bulk shear values averaging about 25 m s^{-1} (50 kt). Both these environmental factors aided in the enhanced risk for severe and rotating thunderstorms. By 0600 UTC, this severe weather was manifest as an organized, linear southwest to northeast oriented boundary of convection that stretched from far southeastern Texas through northern Louisiana up through southeastern Arkansas to the Ohio River Valley, shown in Fig. 7.

d. 11-12 March 2016

The upper-level low began to slowly move to the northeast, with the 300 hPa jet streak still rounding the base of the trough at 0000 UTC 11 March 2016 with only slight weakening in the magnitude of the winds (Fig. 8a). The 500 hPa center was located on the Texas/Mexico border near Brownsville as illustrated in Fig. 8b. Despite the upper-level trough continuing to move to the northeast, the associated 1470 m geopotential height minimum at 850 hPa (Fig. 8c) seems quasi-stationary along the western Gulf of Mexico and Mexico/Texas coast. The moist air mass ushered northward on the eastern side of this weak low pressure center continued to fuel heavy rainfall while maintaining instability and an elevated risk of severe thunderstorms and isolated tornadoes in the south-central U.S due to CAPE values in the region around 800 K kg^{-1}. The line of convection that developed a day earlier continued to push eastward and now extended from southeast Louisiana into central portions of Mississippi and northwestern portions of Alabama, all the way up through the Ohio River Valley and lingered into the northeastern U.S (Fig. 9). The former closed surface cyclone opened back into an open wave, with a broad surface trough located across the

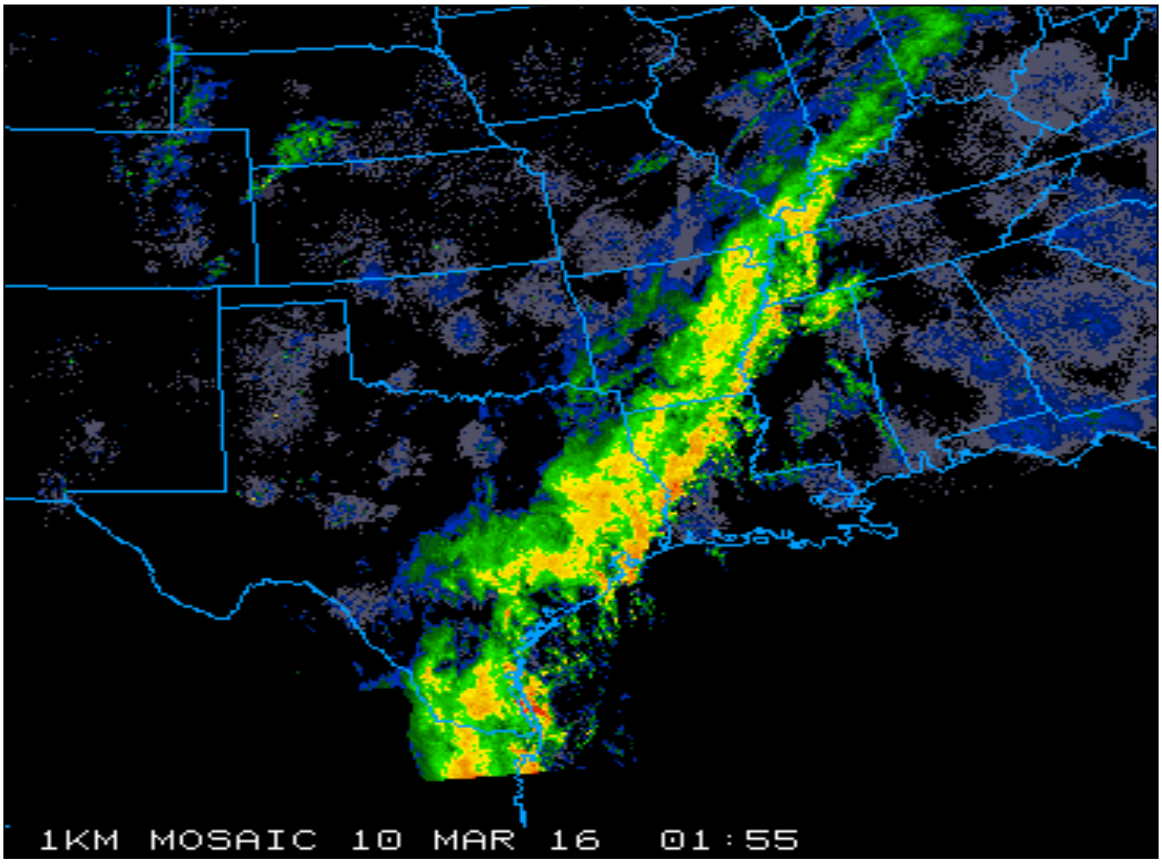

Figure 7. Radar image taken at 01:55 UTC on 10 March 2016. Data provided by UCAR.

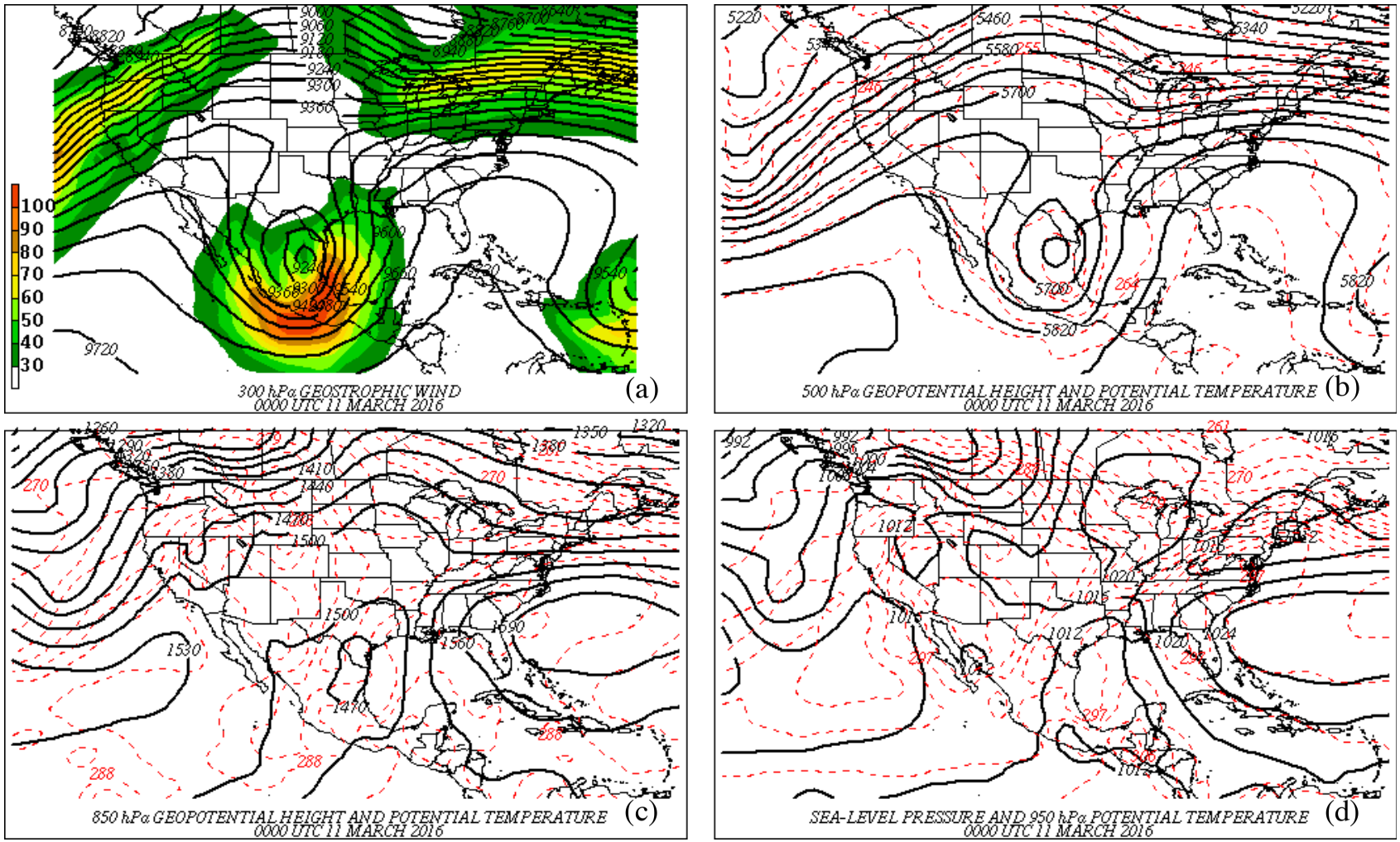

Figure 8. 0000 UTC 11 March 2016 (a) 300 hPa geopotential heights (solid black contour) contoured every 60 m and geostrophic isotachs (shaded) beginning at 30 m s^{-1} in 10 m s^{-1} increments (b) 500 hPa geopotential heights (solid black contour) contoured every 60 m and isentropes (red dashed) every 3 K (c) 850 hPa geopotential heights (solid black contour) contoured every 30 m and isentropes (red dashed) every 3 K (d) Sea-level pressure (solid black contour) contoured every 4 hPa and 950 hPa isentropes (red dashed) contoured every 3 K.

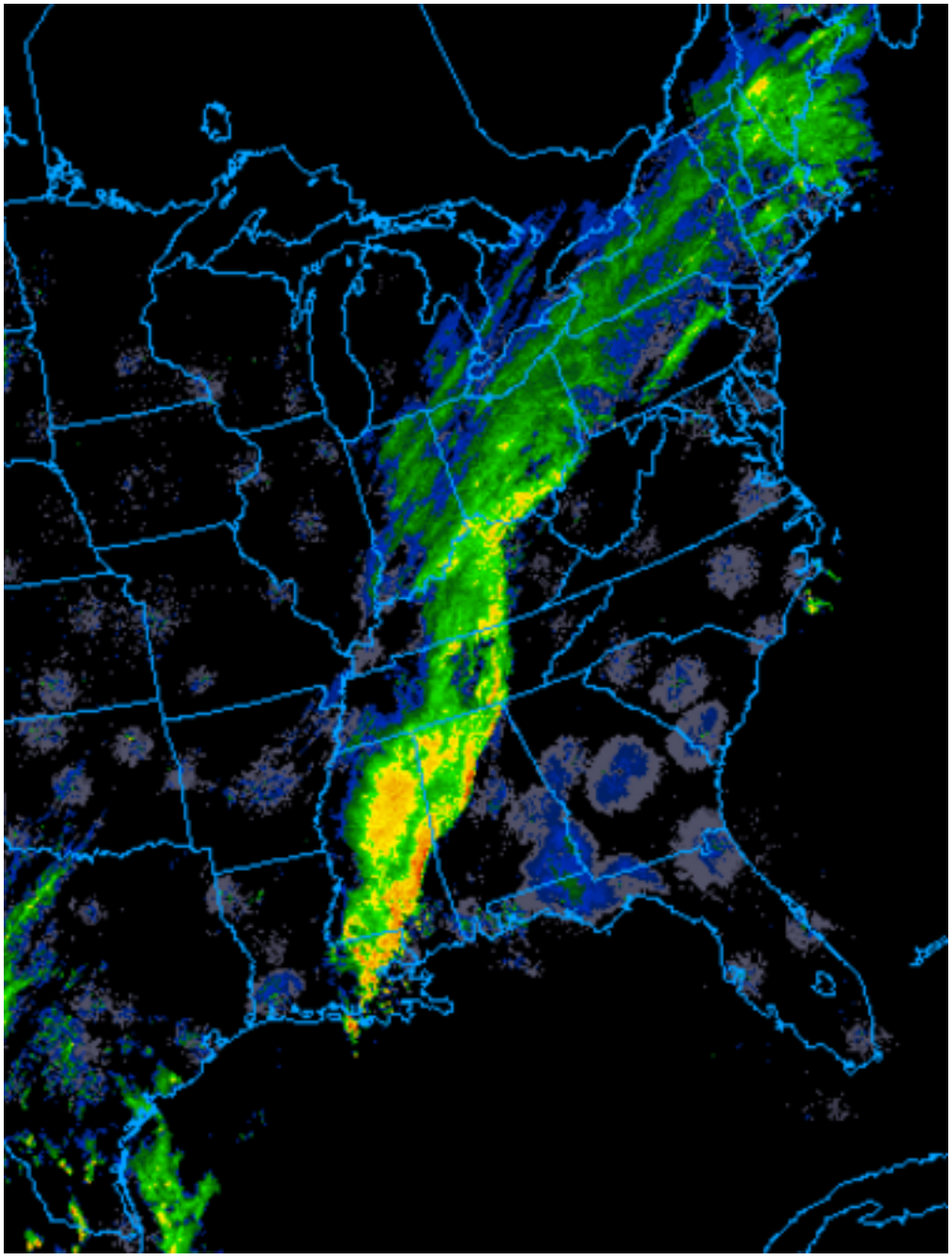

Figure 9. Radar image taken at 24:55 UTC on 10 March 2016. Date provided by UCAR.

Gulf of Mexico, as depicted in Fig. 8d. By 1200 UTC, most of the southcentral U.S. was again being inundated with rainfall from convection being driven northward off of the Gulf of Mexico and into the southcentral U.S.

The slow moving 500 hPa closed cutoff low continued to drift to the northeast and by 0000 UTC 12 March was located over Brownsville, TX (Fig. 10b) ahead of a new upper-level trough beginning to dive southward into southern California. Figure 10a shows that a broad 40-60 m s^{-1} 300 hPa geostrophic jet streak became wrapped around and embedded within the upper-tropospheric trough at this time, emphasizing its still cut-off nature. There was also minimal signature of a closed cyclone appearing at 850 hPa as compared to upper levels (Fig. 10c), since becoming an open wave a day earlier. This weakening trend continued throughout the following days, eventually dissipating as it moved to the northeast towards the lower and mid-Mississippi Valley (not shown). However, a large area of enhanced low-level moisture advected from the Gulf of Mexico associated with its passing converged in the southcentral U.S. and resulted in another day of widespread convection. However, ample cloud cover ensured that most of the convection that developed was below severe thresholds (not shown).

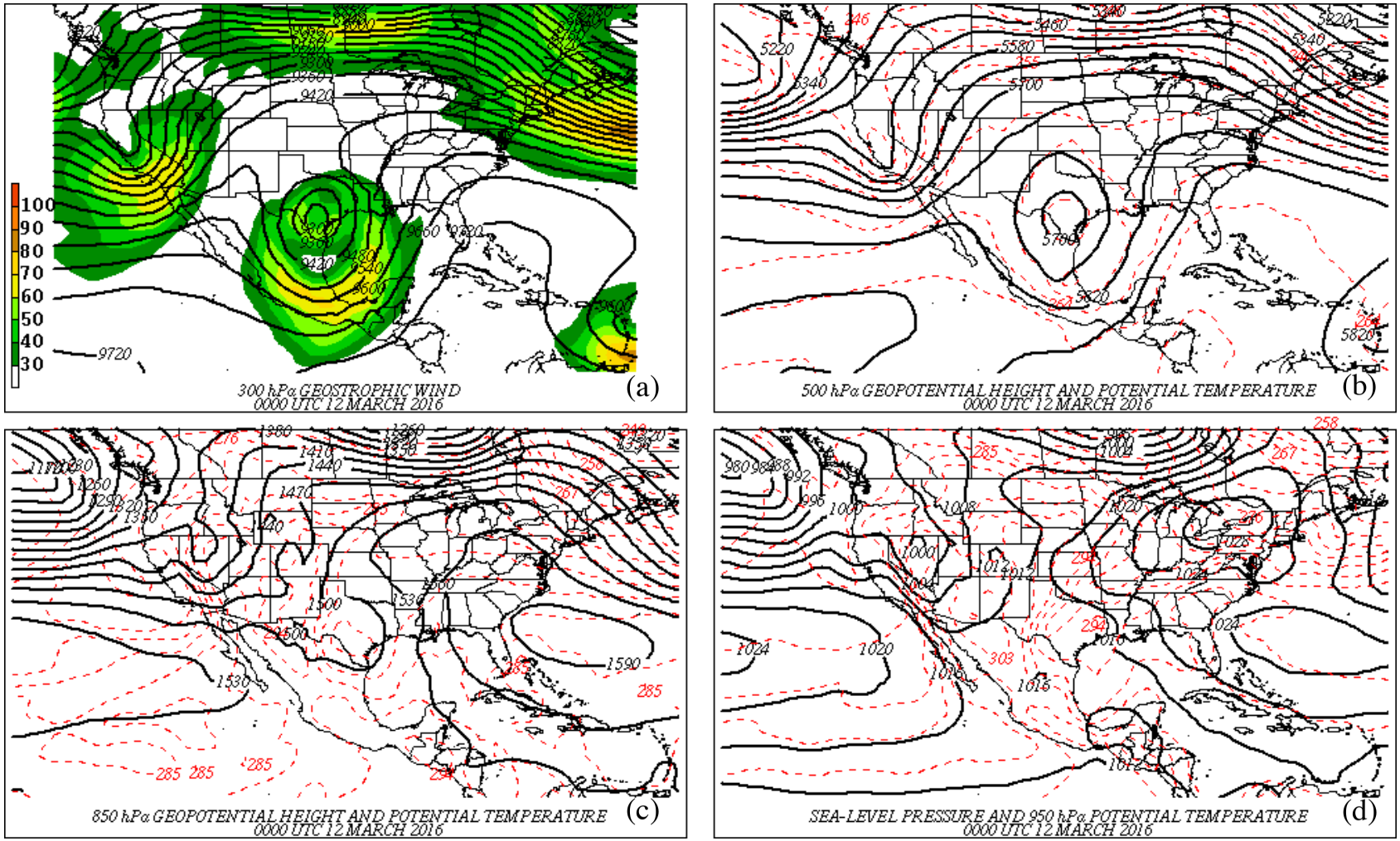

Figure 10. 0000 UTC 12 March 2016 (a) 300 hPa geopotential heights (solid black contour) contoured every 60 m and geostrophic isotachs (shaded) beginning at 30 m s^{-1} in 10 m s^{-1} increments (b) 500 hPa geopotential heights (solid black contour) contoured every 60 m and isentropes (red dashed) every 3 K (c) 850 hPa geopotential heights (solid black contour) contoured every 60 m and isentropes (red dashed) every 3 K (d) Sea-level pressure (solid black contour) contoured every 4 hPa and 950 hPa isentropes (red dashed) contoured every 3 K.

2. METHODOLOGY

2.1 Data

This study is performed using global model analyses from the National Center for Environmental Prediction (NCEP) Final (FNL) Operational Model Global Tropospheric Analyses of the flooding event 08-12 March 2016 evaluated within the General Meteorological Package (GEMPAK) and Matrix Laboratory (MATLAB). This data is on a 1° x 1° horizontal grid, with 20 vertical levels between 1000 hPa and 50 hPa in 50 hPa intervals. The data is available at 6-hourly analysis intervals, at 0000 UTC, 0600 UTC, 1200 UTC, and 1800 UTC. The analyses are produced about an hour after the Global Data Assimilation System (GDAS) produces the real-time "early run" analysis, and thus includes more observations than the real-time analysis. Full Global Forecast System (GFS) model dynamics and information can be found on the NCAR FNL dataset description page[6].

The study also uses the Climate Forecast System Reanalysis (CFSR) dataset (Saha et al. 2010) that includes data from 1979- 2010. It was used solely to calculate the standardized anomalies of the geopotential heights during the 08-12 March 2016 event over the 31-year period. The CFSR is a global, high resolution, coupled atmosphere-ocean-land surface-sea ice system. It generates variable information at 6-hour time intervals, at 0.5° x 0.5° horizontal grid spacing, and on the same pressure levels as the GFS analysis, making it a convenient dataset to work with when developing a climatology. Additional information relating to this model can be found at the NCAR climate data CFSR website[7].

---

[6] https://rda.ucar.edu/datasets/ds083.2/

[7] https://climatedataguide.ucar.edu/climate-data/climate-forecast-system-reanalysis-cfsr.

2.2 Sawyer–Eliassen Circulation Equation

One aspect of the March 2016 case that makes it interesting is the apparent development of an upper-level front in northwesterly flow, and its role on the deepening of the upper-level trough. Though the role and influence of upper-level fronts have been studied intensely in the past via other case studies, the possible influence of an upper-level front in relation to this case study has yet to be investigated. Thus, this study aims to investigate if and how an upper-level front may have contributed to the lowering of the 500 hPa geopotential heights. Consequently, this research will utilize the Sawyer–Eliassen circulation diagnostic to examine the development of the upper-level front which had an influence on the upper-level trough.

Figure 11 shows a region of geostrophic cold air advection in cyclonic shear at 400 hPa at 0000 UTC 08 March, as emphasized by the shaded region located upstream of the trough axis, along with the corresponding geopotential heights and isentropes. As previously mentioned, this location is optimal for the development of an upper-level front. Thus, a cross-section from A_1 located in the south-central Pacific Ocean to A_2 located on the border of Nevada and Wyoming was taken perpendicular to the isotherms across the jet in the region of geostrophic cold air advection, and the Sawyer–Eliassen circulation solver was utilized.

This study implements a Sawyer–Eliassen circulation equation solver developed and described by Winters and Martin (2014). The Sawyer–Eliassen circulation equation (1) is given by:

$$\left(-\gamma\frac{\partial\theta}{\partial p}\right)\frac{\partial^2\psi}{\partial y^2}+\left(2\frac{\delta M}{\delta p}\right)\frac{\partial^2\psi}{\partial p\delta y}+\left(-\frac{\partial M}{\partial y}\right)\frac{\partial^2\psi}{\partial p^2}=Q_g-\gamma\frac{\partial}{\partial y}\left(\frac{d\theta}{dt}\right) \quad (1)$$

where $\gamma = \frac{R}{fp_0}(\frac{p_0}{p})^{\frac{c_v}{c_p}}$, p_0 = 1000 hPa, *R* is the gas constant for dry air, c_v= 718 J kg^{-1} (the specific heat capacity with respect to volume), and c_p = 1004 J kg^{-1} K^{-1} (R + c_v). M is the absolute geostrophic momentum (M = U_g –fy), where U_g and V_g are the along- and across-

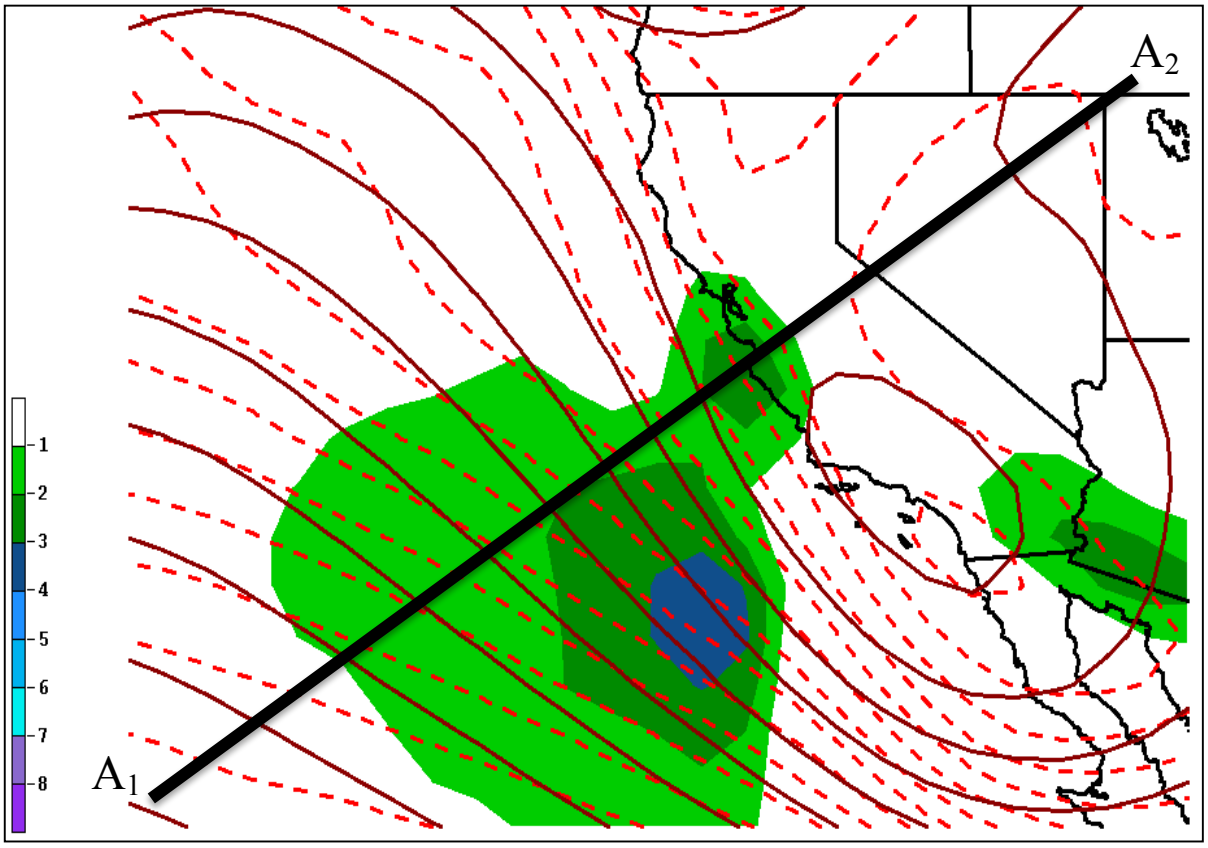

Figure 11. 0000 UTC 08 March 2016. 400 hPa geostrophic cold air temperature advection (shaded) in units of K s^{-1}, geopotential heights (solid) contoured every 60 meters and potential temperature (dashed) contoured every 2 K. Circled is region of geostrophic cold air advection in cyclonic shear. Cross-section between A_1 and A_2 used in Sawyer-Eliassen Solver.

front geostrophic winds, respectively, Q_g is the geostrophic forcing function also written as: $Q_g = \frac{\partial U_g}{\partial y}\frac{\partial V_g}{\partial p} - \frac{\partial V_g}{\partial y}\frac{\partial U_g}{\partial p}$, and θ is the potential temperature. It is important to note that the geostrophic forcing function is the sum of the shearing (QSH = $2\gamma[(\partial \mathrm{Ug}/\partial \mathrm{y})(\partial\theta/\partial \mathrm{x})]$) and stretching deformation (QST = $2\gamma[(\partial \mathrm{Vg}/\partial \mathrm{y})(\partial\theta/\partial \mathrm{y})]$) terms. The three coefficients of the second-order terms on the left-hand side of the equation represent the static stability, baroclinicity, and inertial stability, respectively (Winters and Martin 2014). Overall, this is a linear, second-order partial differential equation that describes the two-dimensional non-divergent ageostrophic flow in the two-dimensional plane perpendicular to the frontal zone via the Sawyer–Eliassen streamfunction, ψ, such that $v_{ag} = -\partial\psi/\partial p$ and $\omega = dp/dt = \partial\psi/\partial y$. The equation describes semi-geostrophic cross-frontal diagnosis, due to the fact that it includes across-front, ageostrophic advections of temperature and momentum. As Winters and Martin 2014 explain, the second-order nature of the differential equation means that positive (negative) values for the forcing function correspond to the minimum (maximum) values for the streamfunction and thermally direct (indirect) circulations. The reader is referred to Eliassen (1962) for full derivation of the Sawyer (1956) – Eliassen (1962) equation.

To solve the Sawyer–Eliassen equation, the distribution of the variables listed above must first be defined. Thus, the absolute temperature, geostrophic winds, vertical motion, and relative humidity values are taken from the analyses from 1000 hPa to 50 hPa at 50 hPa vertical intervals. These values are then interpolated onto the cross section line shown in Fig. 11. Consequently, all of the coefficients and forcing functions in the Sawyer–Eliassen

circulation equation can then be solved based on the interpolation of these variables at each grid point. The rate of latent heating, $\frac{d\theta}{dt}$, can be calculated using the method of Emanuel et al. (1987) via

$$\frac{\mathrm{d}\theta}{\mathrm{dt}} = \omega\left(\frac{\partial\theta}{\partial \mathrm{p}} - \frac{\Gamma_m}{\Gamma_d}\frac{\theta}{\theta_e}\frac{\partial\theta_e}{\partial p}\right) \quad (2)$$

where θ_e is the equivalent potential temperature, ω is the diagnosed analysis vertical motion, Γ_m is the moist-adiabatic lapse rate, and Γ_d is the dry-adiabatic lapse rate.

After all of the forcing terms have been calculated, a successive over-relaxation technique is used to diagnose the Sawyer–Eliassen streamfunction. This type of technique is iterative - continuing to repeat and advance toward a solution until one is obtained relative to a chosen threshold criteria for convergence. However, a unique solution can only be obtained if the QGPV is greater than zero at each grid location in the solution domain. If this is not the case, then it must mean that there is either inertial or static instability somewhere in the domain that would "allow for the growth of non-unique solutions arising from the release of instability, thus prohibiting clear attribution of the resulting ageostrophic motions to the process of frontogenesis" (Martin 2006). To avoid this dilemma, if any grid points have values of QGPV that are less than zero, the successive over-relaxation technique calculates the Sawyer–Eliassen streamfunction at neighboring grid points and uses a four-point average of these streamfunction values that is then assigned to the omitted grid point. It is important to note that in accordance with the techniques detailed by Todsen (1964) and Shapiro (1981), the Sawyer–Eliassen streamfunction is initialized in the domain, with the Dirichlet boundary conditions fixed at zero throughout the entire iteration process. It is important to mention

that the solver code demands that the cross section be aligned along grid point locations (eg. zonally, meridionally, NW to SE or NE to SW oriented only) in order interpolate data to the cross-sectional plane and execute. The latitude and longitude bounds of the cross section, rounded to nearest whole numbers, as well as the calculated variables mentioned above, were input to the solver.

2.3 The Piecewise Static Quasigeostrophic Potential Vorticity Inversion

a. Technique and Definitions

The quasigeostrophic potential vorticity q, is defined as follows via Charney and Stern (1962):

$$q = f + \frac{1}{f_0}\nabla^2\varphi + f_o\frac{\partial}{\partial p}\left(\frac{1}{\sigma}\frac{\partial\varphi}{\partial p}\right) = f + \mathcal{L}(\phi) \quad (3)$$

where pressure is the vertical coordinate and f, f_0, and σ are the Corilois parameter, the reference Coriolis parameter (10^{-4} s^{-1}), and static stability, respectively. One of the most useful properties of PV is its ability to be inverted via suitable boundary conditions (Hoskins et al. 1985) to obtain the geopotential φ field from the q field (Nielsen-Gammon and Lefevre 1996). This relationship is expressed below:

$$\varphi = \mathcal{L}^{-1}(q - f) \quad (4)$$

To successfully use this inversion technique, q on the interior of the domain and θ along the upper and lower boundaries must be specified. The upper and lower boundaries are defined using the boundary potential temperature as follows:

$$\frac{\partial\varphi}{\partial p} = -\frac{R}{p}\left(\frac{p}{p_0}\right)^{\frac{R}{c_p}}\theta \quad (5),$$

whereas the vertical boundaries are defined using the Neumann boundary conditions.

As Hakim et al. (1996) describe, QGPV inversion allows for the total flow field to be portioned in a dynamically meaningful way that allows for quantitative analysis of the individual roles of precursor disturbances in the evolution of a given case. Use of this technique requires the full QGPV be partitioned first into its respective mean and perturbation fields (as described in the following subsection). Once identified, the full perturbation field can then be further partitioned into any number of discrete QGPV anomalies, each of which are associated with specific mass and momentum fields (Hoskins et al. 1985; Davis and Emanuel 1991) presumably of synoptic-scale dynamical interest. This is referred to as the piecewise static QGPV inversion.

b. Mean and Perturbation Fields

Effective use of the piecewise QGPV inversion requires a meaningful partitioning of the *perturbation* QGPV. To use the QGPV inversion technique, the mean and perturbation fields must first be determined, where

$$q = \bar{q} + q' \quad (6)$$

$$\varphi = \bar{\varphi} + \varphi' \quad (7)$$

While any arbitrary state can be defined as the basic state, the choice of a mean state drastically affects the outcome and interpretation of the perturbation QGPV, and is thus extremely important to define. For example, Nielsen-Gammon and Lefevre (1996) declare that the most common time mean basic state is calculated over an interval long enough to encompass at least one period of the waves of interest. In addition, they mention that failing to choose an adequate basic state mean that will isolate the system from other large scale features will, for instance, result in inaccurate representations of height changes that do not

realistically mimic the intensification or weakening of the overall system. Thus, in order to most effectively analyze this case, the time mean was chosen following a technique similar to that described in Martin and Marsili (2002), in which the time mean is defined by the six days that bookend the event of interest. In other words, the time mean was the average of the six days from 05-07 March 2016 and 13-15 March 2016. In this way, the features of interest in the PV field are isolated and placed strictly in the perturbation field during the time period of 08-12 March. The mean QGPV so defined was then subtracted from the instantaneous QGPV distribution at each discrete time in the analysis. This difference field is referred to as the perturbation QGPV for that specific time.

There are two main goals for the partitioning process: the first is to account for as much of the perturbation QGPV field as possible, without inverting any of it more than once, and the second is to select the fewest number of partitions that adequately describe the feature of interest (Martin and Marsili 2002). Theoretically, using this separation technique would provide a framework to quantify cause- and effect interactions between discrete entities (Hakim et al. 1996). Thus, a specific partitioning scheme similar to those described by Hakim et al. (1996) and Nielsen-Gammon and Lefevre (1996) was utilized. The first partition is referred to as the lower layer $\mathbf{L_{PERT}}$, and extends from 1000 hPa to 550 hPa. This layer was developed to find QGPV in the lower to mid troposphere. The second layer, referred to as the upper layer $\mathbf{U_{PERT}}$, extends from 500 hPa to 50 hPa and was specified to isolate QGPV anomalies in the middle to upper troposphere. This convention is summarized by:

$$\varphi'_{total} = \varphi'_{upper} + \varphi'_{lower} = \mathcal{L}^{-1}(q'_{upper}) + \mathcal{L}^{-1}(q'_{lower}) \quad (8)$$

It is important to note that the QGPV at all levels above the lower layer were set to zero when performing the lower layer inversion, and similarly the QGPV at all levels below the defined upper level layer were set to zero when performing the upper level QGPV inversion. After utilizing this separation technique and performing the inversion, the relative influences of the discrete upper or lower level QGPV anomalies on the 500 hPa (or any other level) geopotential height changes can be quantitatively assessed.

2.4 QGPV Inversion and Poleward Geostrophic Moisture Flux

Prior studies of extreme rainfall cases have shown that moisture flux convergence from the Gulf of Mexico over the south-central U.S is one of the main contributing factors to the high rainfall totals (Lackmann and Gyakum 1999; Winters and Martin 2014). As previously mentioned, understanding the PGMF is an important goal of this research. A study by Lackmann and Gyakum (1999) used the same QGPV inversion technique developed by Hakim et al. (1996) to isolate moisture transport associated with specific QGPV anomalies for a cold-season flooding event in the northwestern U.S., assuming that the geostrophic moisture flux approximates the total model moisture flux. To better understand the role of low-level moisture flux over the south-central U.S. in the case of the March 2016 flooding event, this study will use QGPV inversion to answer whether the upper or lower level QGPV anomalies had a larger influence in contributing to the overall lower tropospheric (850 hPa) moisture flux at 0000 UTC 10 March. The total PGMF is defined in this study in a manner similar to that employed by Winters and Martin (2014) and Lackmann and Gyakum (1999) as the product of both the meridional component of the geostrophic wind (v_g) and the instantaneous mixing ratio, q_w:

$$PGMF = (v_g)(q_W) \text{ (9)}$$

This total PGMF can first be separated into its mean and perturbation components:

$$\overline{PGMF} = \overline{v_g q_W} \text{ (10)}$$

$$(PGMF)' = (v_g q_W)' \text{ (11)}$$

and then a final partitioning of the perturbation PGMF into that caused by the upper-level QGPV anomaly and that caused by the lower-level QGPV anomaly is calculated:

$$(PGMF)'_{total} = (PGMF)'_{upper} + (PGMF)'_{lower} \text{ (12)}$$

It is hypothesized that the PGMF associated with the upper-level QGPV anomaly will be larger in magnitude than that associated with the lower-level QGPV anomaly due to the presumed larger influence of the upper-level QPGV anomaly on the overall circulation associated with the trough.

Through the utilization of both the Sawyer–Eliassen and QGPV inversion diagnostics, better insight into the physical mechanisms that drove the south-central U.S. flood of March 2016 is sought.

3. RESULTS

3.1 Sawyer–Eliassen Circulation

This section presents an overview and analysis of the upper-level front and its respective ageostrophic circulation that developed in geostrophic cold air advection in cyclonic shear on 0000 UTC 08 March. Figure 12 depicts these results. Immediately noticeable on the figure is the presence of an upper-level front as evident by the sloping bundle of isentropes from about 330 hPa to 700 hPa. Also noticeable is a 70 m s^{-1} jet maximized at about 250 hPa with a region of maximized geostrophic cold air advection around 4-6 K s^{-1} located to the cyclonic shear side of this jet. As previously mentioned, along-front geostrophic cold air advection in cyclonic shear acts to center the upper-level subsidence directly beneath the jet core (Martin 2014). This subsidence can subduct higher PV from the lower stratosphere into the middle- and upper-troposphere. The analysis presented is consistent with this theory, as it shows subsidence of ~1-3 dPa s^{-1} located directly below the 70 m s^{-1} jet core, and a trench of PV isertels (2-8 PVU) reaching a lowest altitude of about 500 hPa collocated in the region of maximum subsidence.

Figure 13 also analyzes the ageostrophic circulation associated with this upper-level front. This figure is plotted along the same cross-section from A_1 to A_2, but focuses on the solution to the Sawyer–Eliassen circulation equation resulting from the solver described previously. The solution shows a strong thermally direct circulation, as indicated by the negative streamfunction, with a minimum streamfunction value of -2100 m hPa s^{-1}. This circulation then promoted the aforementioned subsidence seen directly beneath the jet core, which according to previous research, aids to promote tilting frontogenesis by increasing the slope of the isentropes and hence, strengthening the upper-level front. Both Figs. 12 and 13

present excellent examples of the tilting frontogenesis theory and help to explain some of the atmospheric dynamics that were involved early in the development of the anomalous March 2016 upper-level trough.

Though the previous analyses provided insight into the development of an upper-level front and its effects via a cross-sectional analysis, the subduction of PV into the middle- and upper-troposphere as a result of the ageostrophic subsidence and its influence on the upper-level trough can also be analyzed from a horizontal perspective. Figure 14 shows the 400 hPa geopotential heights and PV distributions in the 350-450 hPa layer at different times early in development of the upper-level trough. At 1200 UTC 07 March (Fig. 14a), PV values of ~4 PVU are located slightly off the west coast of California. While in northwesterly flow and in the early stages of upper-level frontogenesis, the PV is then advected to the southeast and becomes more elongated by 0000 UTC 08 March (Fig. 14b). The cross-section analysis (Fig. 12) also showed subduction of higher PV into the upper-troposphere occurring at this time. While in this northwest flow regime, the high PV can continue to be simultaneously (1) subducted downward into the upper-troposphere and (2) advected to the southeast. The leading edge of positive PV advection is associated with lower the geopotential heights to the southeast via the QGPV height tendency equation, and can help explain the developing geopotential height anomaly of the upper-level trough. By 1200 UTC 08 March (Fig. 14c), the upper-level trough becomes more cut-off from the main westerly flow and the PV distribution becomes more isotropic, but maintains its maximum magnitude of 4 PVU now off the northwest coast

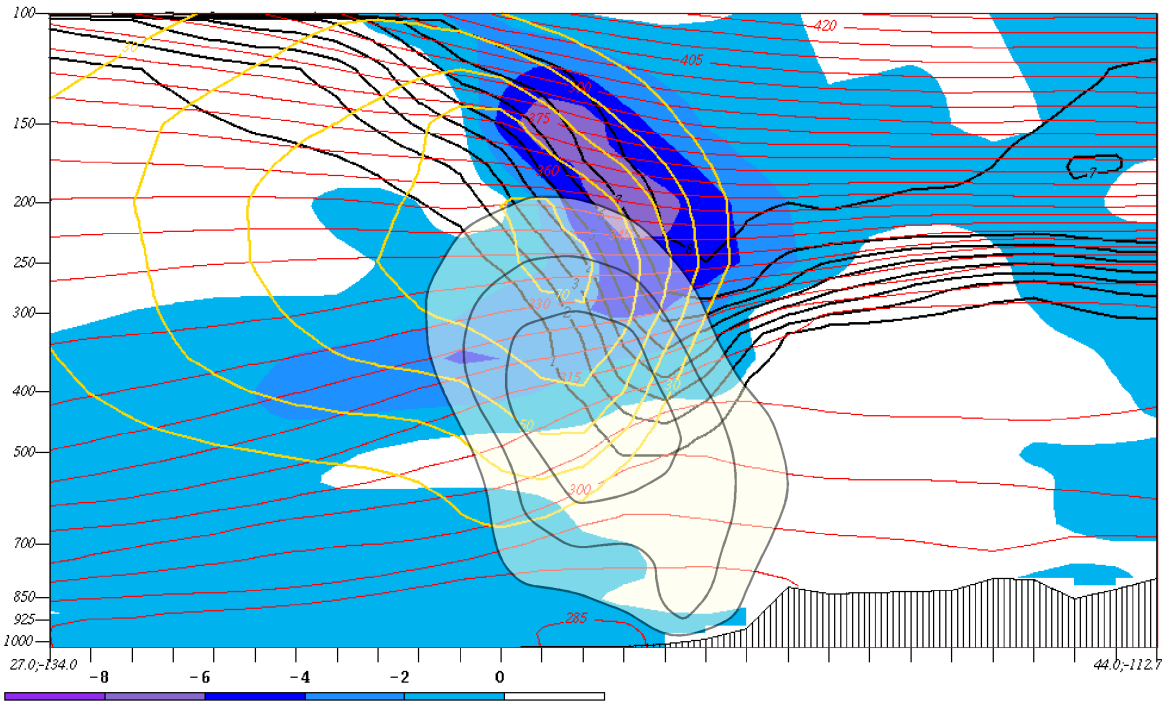

Figure 12. Cross-section between A_1 and A_2 on 0000 UTC 08 March 2016. Geostrophic cold air advection (shaded) every 2 K s^{-1}, isentropes (red solid) contoured every 5 hPa, geostrophic isotachs (yellow solid) contoured ever 10 m s^{-1} starting at 30 m s^{-1}, and positive omega values (black contoured) every 1 dPa s^{-1}.

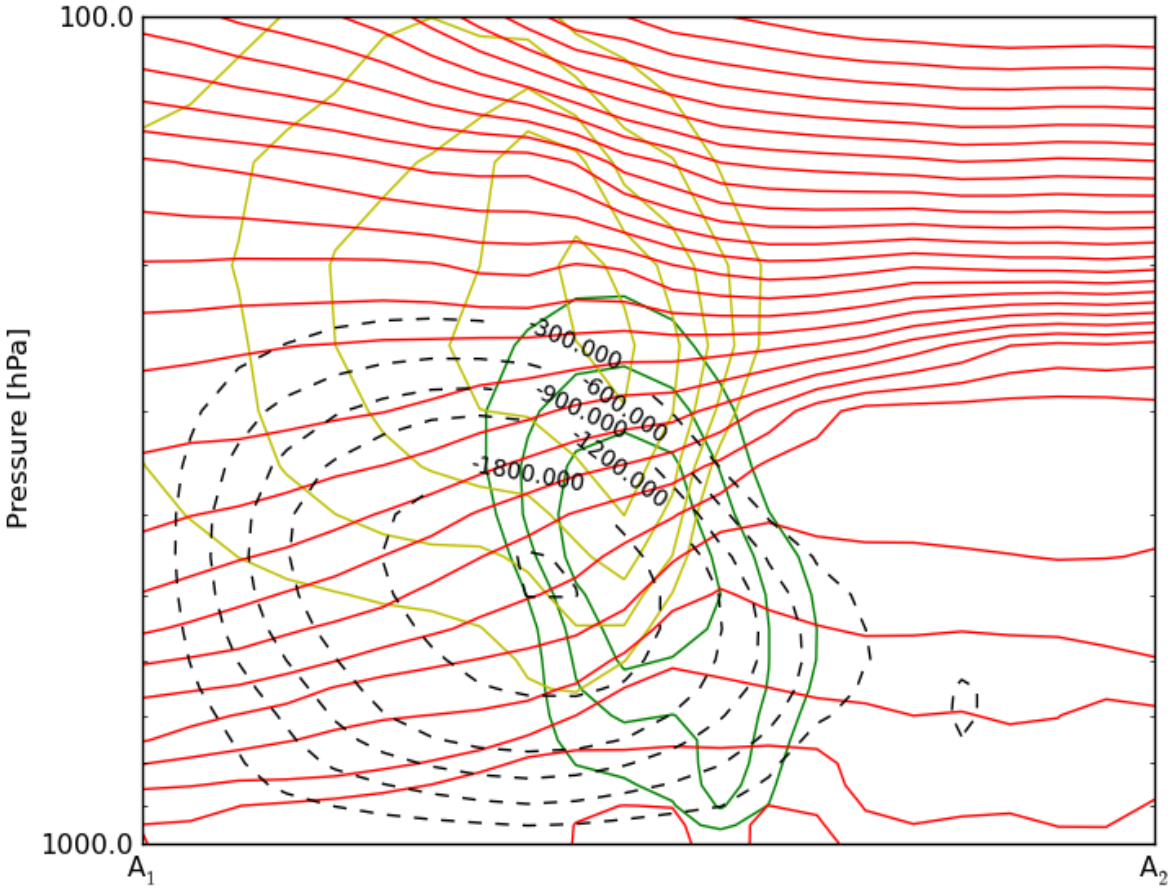

Figure 13. Sawyer-Eliassen Circulation solution in plane of cross-section from A_1 to A_2. Potential temperature (red solid) contoured every 5 hPa, geostrophic isotachs (yellow solid) contoured every 10 m s^{-1} starting at 30 m s^{-1}, positive omega (green solid) contoured every 1 dPa s^{-1}, and Sawyer-Eliassen negative streamfunction every 300 m hPa s^{-1}.

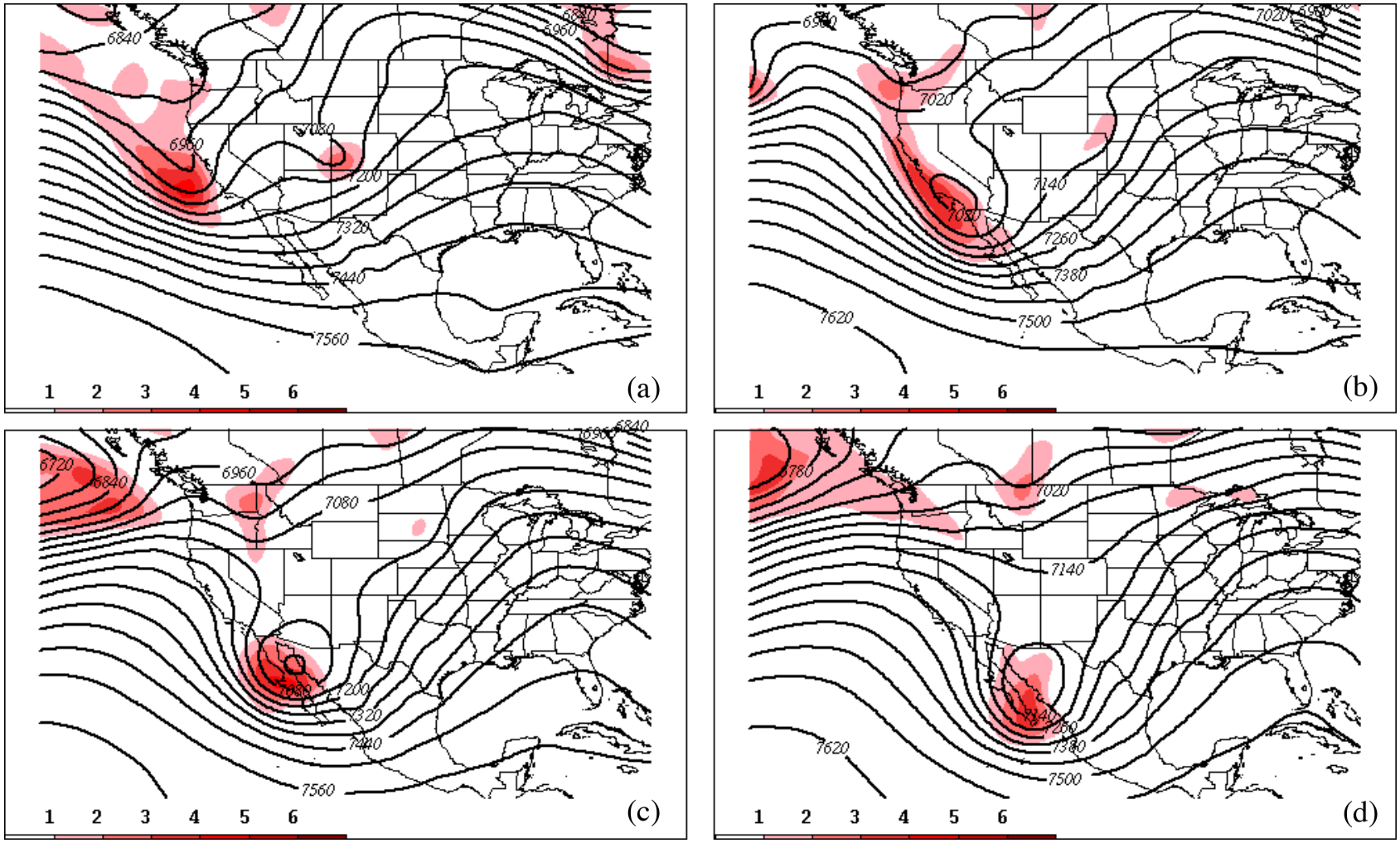

Figure 14. 400 hPa geopotential heights (black solid) contoured every 60 m and 350-450 hPa Layer PV every 1x10^{-6} PVU (red shaded). (a) 1200 UTC 07 March 2016 (b) 0000 UTC 08 March 2016 (c) 1200 UTC 08 March 2016 (d) 0000 UTC 09 March 2016

of Mexico and centered on the Baja California Peninsula. The PV continues to be advected to the southeast over the following 24 hours while in continued northwesterly flow and by 0000 UTC 09 March 2016 (Fig. 14d), the PV becomes nearly collocated with the trough axis. Due to the fact that the PV is only marginally in northwesterly flow at this time, PV advection to the southeast is no longer substantial - suggesting a cessation of the southeastward propagation of the feature. This suggestion is then confirmed via the prior synoptic evolution analysis that showed the upper-level trough reaching its most southern location of about 37°N at 0000 UTC 10 March.

The analysis demonstrates that the development of an upper-level front seemed to have a large influence on the development and propagation of the resulting upper-level trough. Although the Sawyer–Eliassen circulation is a useful diagnostic to qualitatively understand the deformation of the tropopause and stratospheric-tropospheric exchange, it does not provide quantitative information relating to how PV directly influences the upper-level trough. Thus, the following sections aim to accomplish this goal via a static QGPV inversion technique.

3.2. QGPV Inversion Comparisons

One of the goals of this research is to quantitatively study the evolution of the upper-level trough from 08-12 March 2016. To accomplish this goal, the following section presents an overview and analysis of the evolution of 500 hPa geopotential heights obtained from conducting a static QGPV inversion as previously discussed in section 2.3.

a. QGPV Checks

In order to obtain effective and reliable results from the QGPV inversion, a few checks must be made to test the validity of the inversion results when compared to the analysis. It is important to note that the 500 hPa geopotential heights and perturbations from the GFS analyses are considered as "truth" or "reality" for this study, both in magnitude and distribution. The first check involves analyzing the spatial distribution of the 500 hPa geopotential height minimum from the full QGPV inversion when compared to the spatial distribution of the 500 hPa geopotential height minimum seen in the NCEP final analyses. Figure 15 represents the location and intensity of the 500 hPa geopotential height minimum for both the full QGPV inversion and NCEP final analyses, respectively at 12-h intervals from 0000 UTC 08 March to 1800 UTC 12 March. When comparing each 12-h time period, it is evident that the location of the geopotential height minimum associated with both the full inversion and analysis are nearly perfectly geographically collocated in every instance, with the exception of three distinct times at which the separations are negligible. Therefore, it can be claimed that the full QGPV inversion results align well in distribution when compared to the NCEP final analyses over the five-day period.

Another check that must be completed to validate the results of the full QGPV inversion is to compare the magnitude of the 500 hPa geopotential height minimum associated with the full inversion to the magnitude of the 500 hPa geopotential height minimum of the NCEP final analyses. As previously mentioned, Fig. 15 also shows the magnitude of the 500 hPa geopotential height minimum associated with both the full QGPV inversion and the NCEP final analyses from 0000 UTC 08 March to 1800 UTC 12 March in

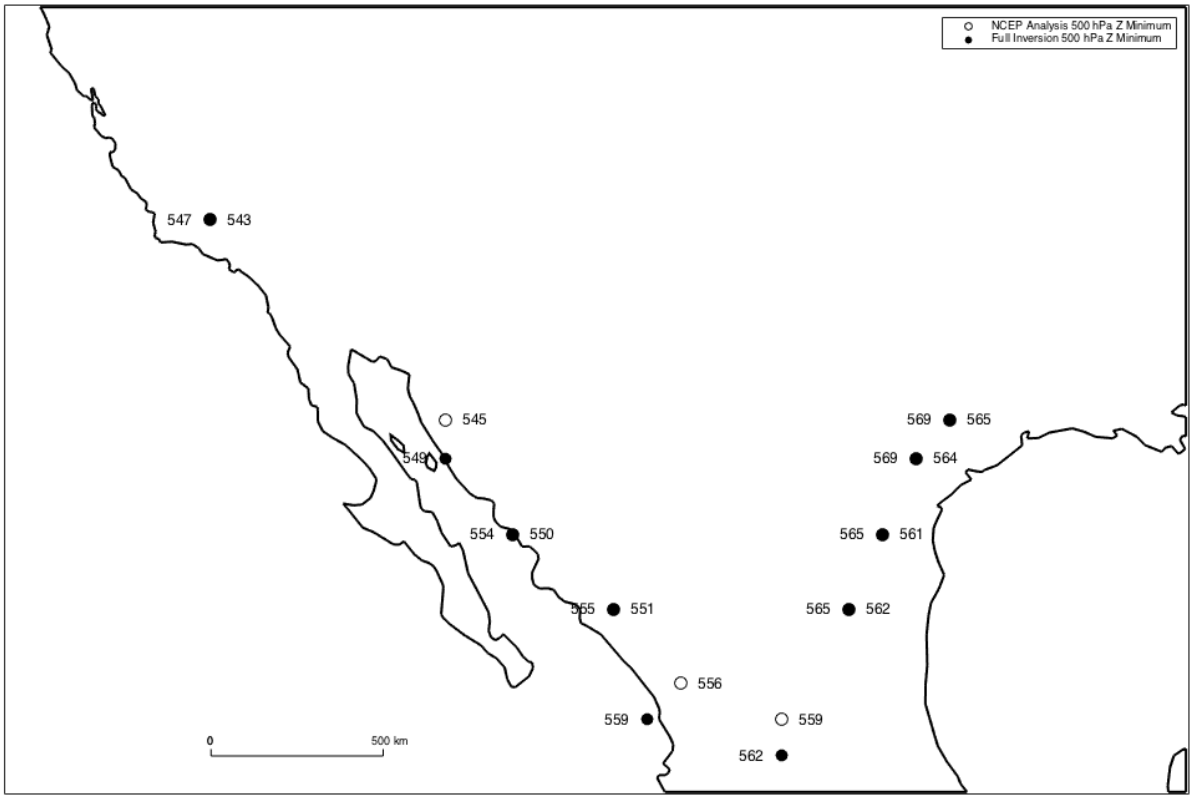

Figure 15. The 12-hourly locations of the 500 hPa geopotential height minima from the NCEP final analysis (open circles) compared to those obtained from the inversion of the full QGPV field (filled circles) from 0000 UTC 08-12 March. Magnitude of the analysis (full inversion) 500 hPa geopotential height minima are given by numbers to the right (left) of the dots in units of dm.

the same 12-h increment. The geopotential height minimum obtained from the full QGPV inversion faithfully reproduces the minimum from the NCEP final analyses throughout the entire time interval, though are uniformly about 1% greater in magnitude than the analyses with a Root Mean Squared Error (RMSE) of ~ 40 m. Thus, it can be claimed that when comparing magnitudes of the geopotential height minimum, the results obtained using the full QGPV inversion at 500 hPa adequately agrees with truth and can be used to assess the evolution of the upper-level trough.

Since the full QGPV inversion geopotential height minimum compare well in both magnitude and distribution with the NCEP final analyses, it can be assumed that any results obtained at the 500 hPa level using the full QGPV inversion can be utilized in this study and analyzed with confidence.

b. Partitioned Full QGPV Inversion Geopotential Heights: Mean and Perturbation

As previously mentioned, the 500 hPa geopotential heights from the full QPGV inversion and the NCEP final analyses are separated into both mean and perturbation geopotential height fields using the arbitrary bookend time mean chosen and discussed in the methodology. Figure 16 shows 12- h intervals of the full QPGV inversion 500 hPa geopotential height perturbation distributions (TOT_{PERT}) from 0000 UTC 08 March until 1200 UTC 12 March. Similar to analysis conducted by Martin and Marsili (2002), the L located on each of these subplots in the figure represents the position of the 500 hPa geopotential height minimum obtained from the full QGPV inversion. Similarly, Fig. 17 shows 12-h intervals of the NCEP final analysis 500 hPa geopotential height perturbations over this same time period, with the L representing the 500 hPa height minimum obtained

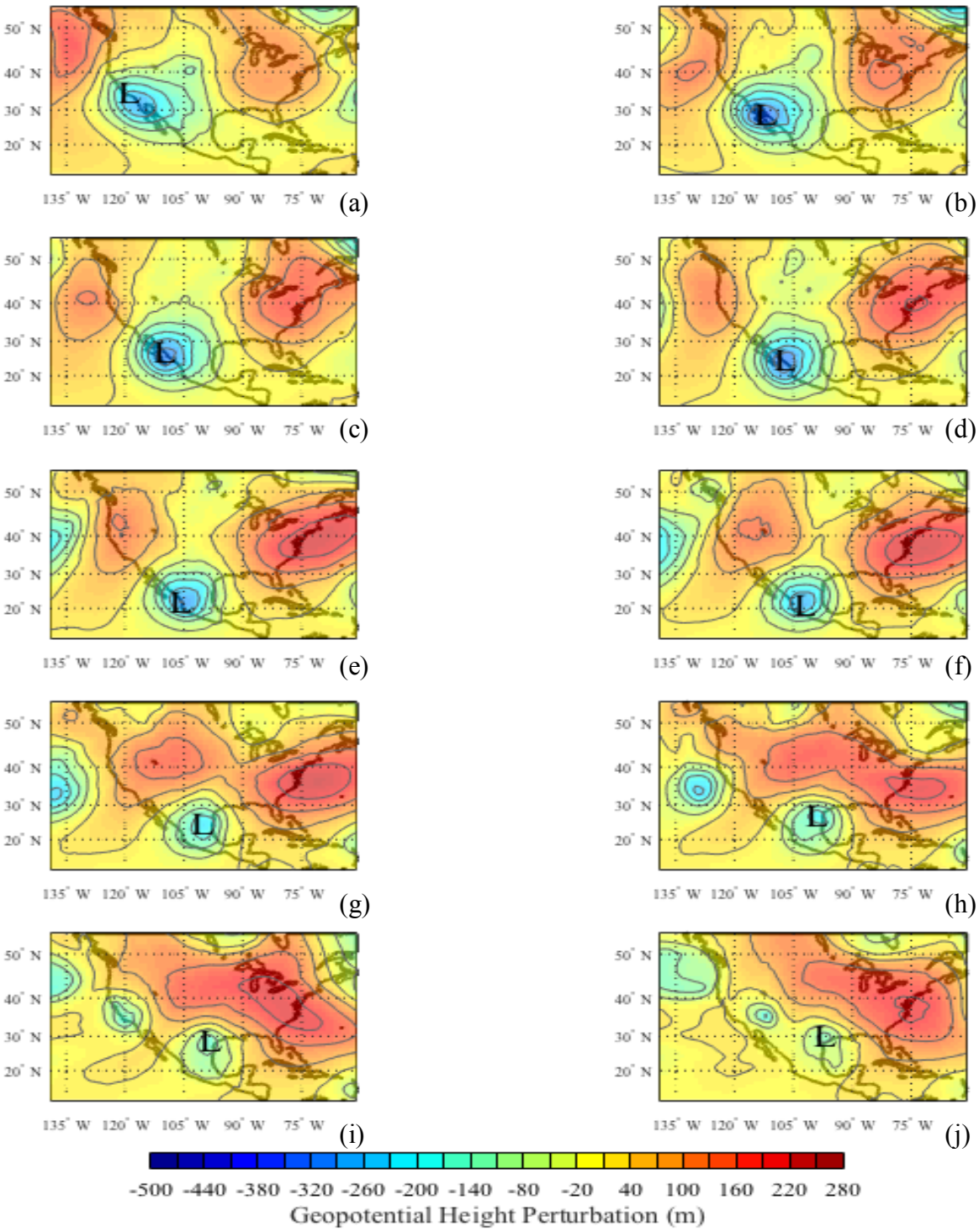

Figure 16. The 500 hPa geopotential height perturbations associated with the TOT_{pert} QGPV anomaly at (a) 0000 UTC 08 March 2016 (b) 1200 UTC 08 March 2016 (c) 0000 UTC 09 March 2016 (d) 1200 UTC 09 March 2016 (e) 0000 UTC 10 March 2016 (f) 1200 UTC 10 March 2016 (g) 0000 UTC 11 March 2016 (h) 1200 UTC 11 March 2016 (i) 0000 UTC 12 March 2016 (j) 1200 UTC 12 March 2016. The L indicates the position of the 500 hPa full inversion geopotential height minimum for each time step.

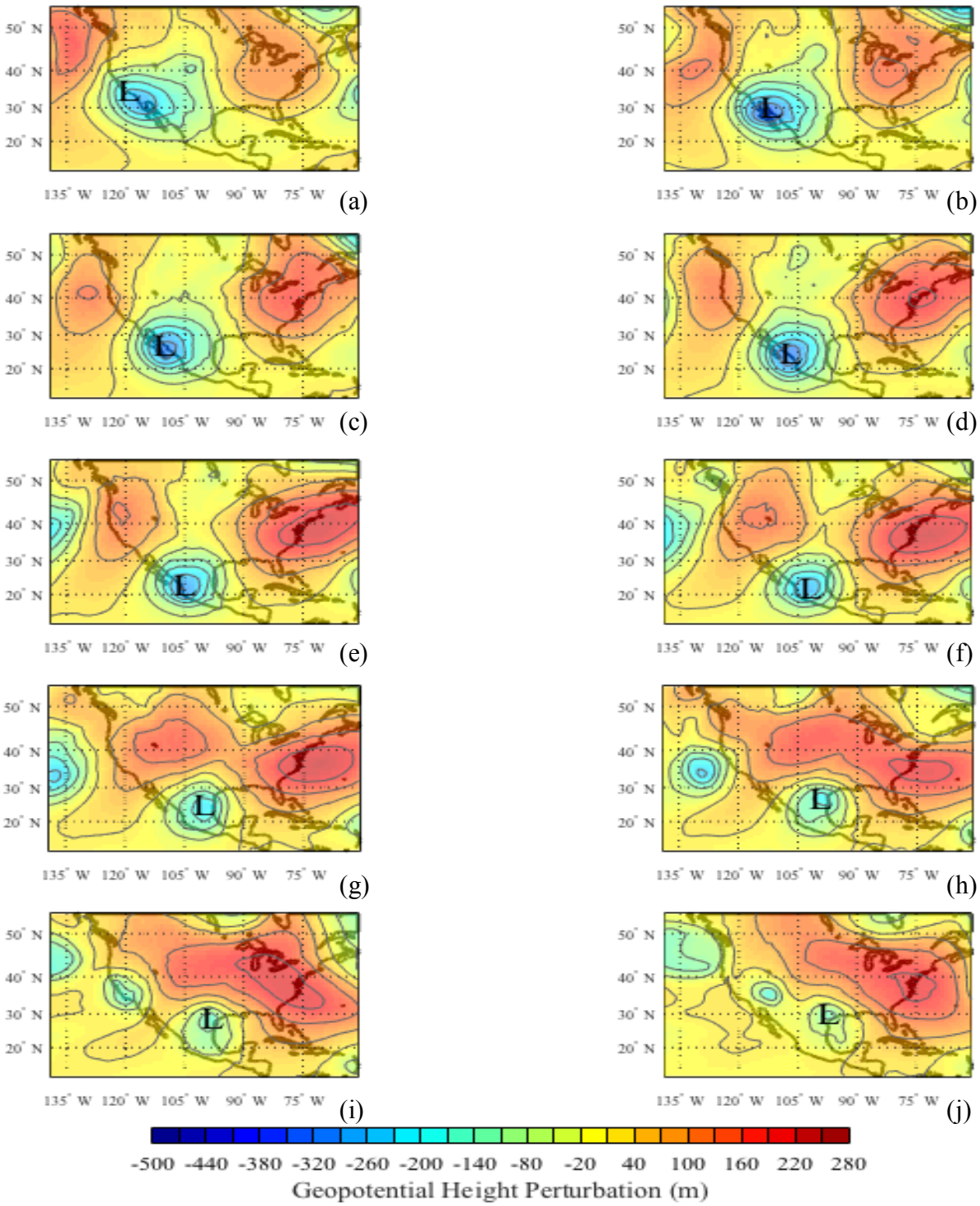

Figure 17. The 500 hPa geopotential height perturbations associated with the NCEP final analysis at (a) 0000 UTC 08 March 2016 (b) 1200 UTC 08 March 2016 (c) 0000 UTC 09 March 2016 (d) 1200 UTC 09 March 2016 (e) 0000 UTC 10 March 2016 (f) 1200 UTC 10 March 2016 (g) 0000 UTC 11 March 2016 (h) 1200 UTC 11 March 2016 (i) 0000 UTC 12 March 2016 (j) 1200 UTC 12 March 2016 . The L indicates the position of the 500 hPa geopotential height minimum for each time step.

from the GFS final analyses. Again, it can be seen that the perturbations associated with the full atmosphere QGPV inversion align well spatially with the perturbations associated with the NCEP final analyses. Based on this qualitative validation of the full QGPV inversion, the partitioning process can then continue by separating TOT_{PERT} into both its respective upper- and lower-layer QGPV anomalies.

c. Partitioned TOT_{PERT}: U_{PERT} and L_{PERT}

The full 500 hPa geopotential height perturbation field associated with the QGPV inversion (TOT_{PERT}) is partitioned into two pieces, with one representing the geopotential height perturbations associated with the upper-level (500-50 hPa) QGPV anomaly (U_{PERT}), and the other representing the geopotential height perturbations associated with the low-level (1000-550 hPa) QGPV anomaly (L_{PERT}). Figures 18 and 19 represent the 500 hPa geopotential height anomalies associated with the U_{PERT} and L_{PERT} QGPV anomalies at 12-hour intervals from 0000 UTC 08 March to 1800 UTC 12 March, respectively. The L located on each of these subplots in both figures represents the position of the 500 hPa geopotential height minimum obtained *solely* from the full QGPV inversion between successive 12-h periods. The magnitude of the 500 hPa geopotential height perturbations at the location of the geopotential height perturbation minima (the L's) for the TOT_{PERT}, U_{PERT}, L_{PERT}, and NCEP final analyses at six-hour intervals over the five-day event are all listed on Table 2. From the table, it is evident that the sum of both the U_{PERT} and L_{PERT} exactly equal the value of TOT_{PERT} at each time. This fact validates the results of the partitioning process and, in essence, was the final "check" that needed to be confirmed.

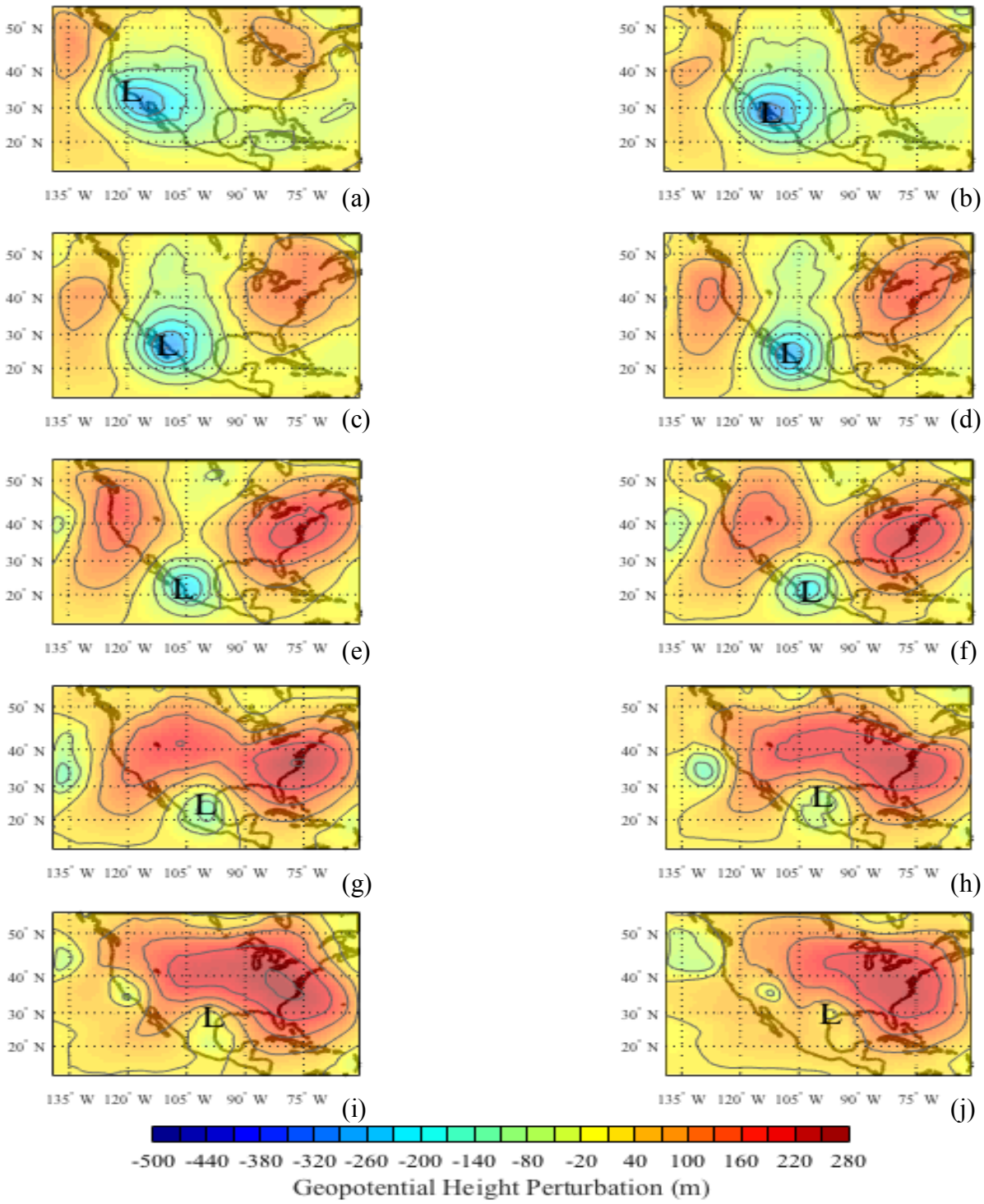

Figure 18. The 500 hPa geopotential height perturbations associated with the U_{pert} QGPV anomaly at (a) 0000 UTC 08 March 2016 (b) 1200 UTC 08 March 2016 (c) 0000 UTC 09 March 2016 (d) 1200 UTC 09 March 2016 (e) 0000 UTC 10 March 2016 (f) 1200 UTC 10 March 2016 (g) 0000 UTC 11 March 2016 (h) 1200 UTC 11 March 2016 (i) 0000 UTC 12 March 2016 (j) 1200 UTC 12 March 2016 . The L indicates the position of the 500 hPa full inversion geopotential height minimum for each time step.

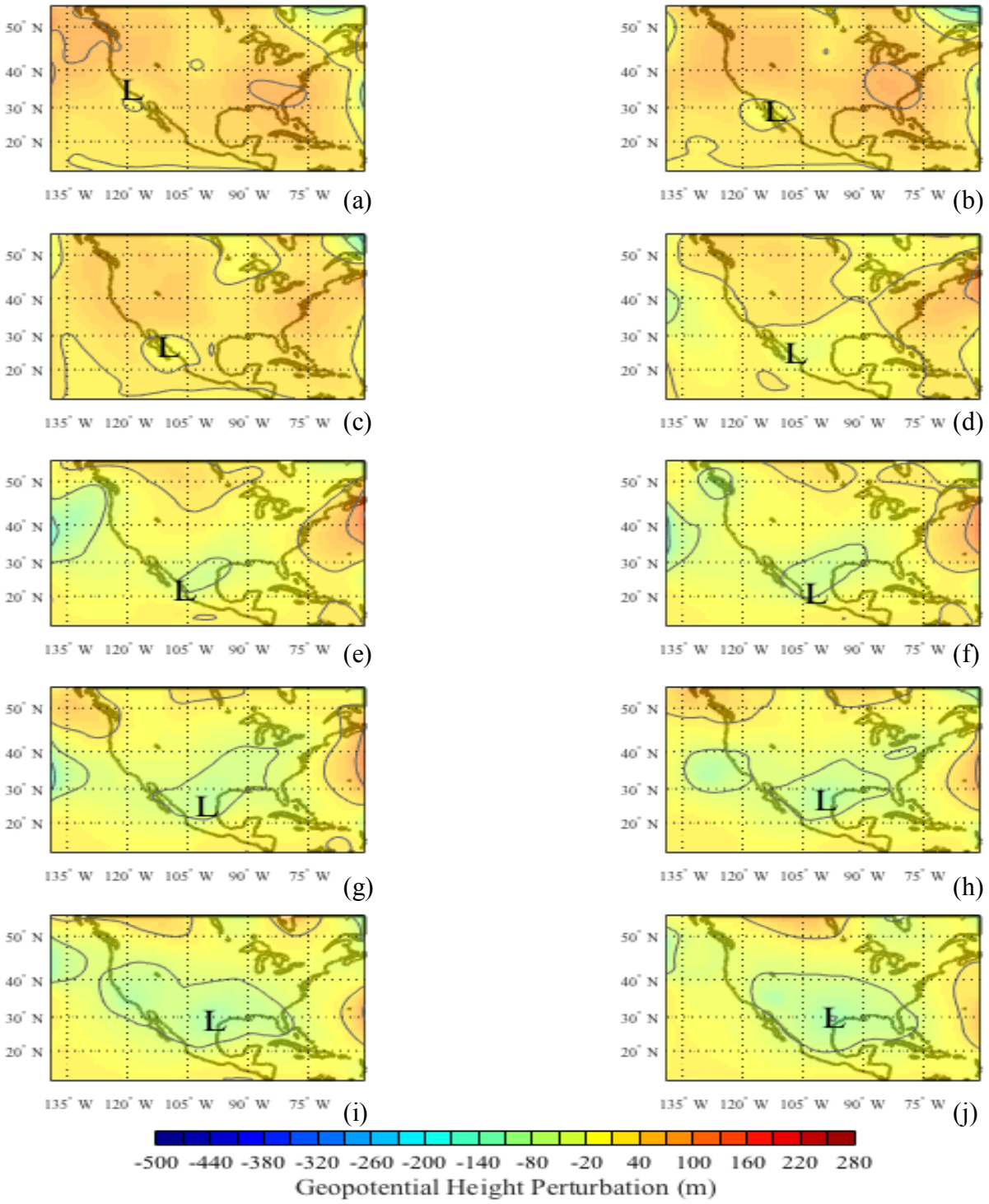

Figure 19. The 500 hPa geopotential height perturbations associated with the L_{pert} QGPV anomaly at (a) 0000 UTC 08 March 2016 (b) 1200 UTC 08 March 2016 (c) 0000 UTC 09 March 2016 (d) 1200 UTC 09 March 2016 (e) 0000 UTC 10 March 2016 (f) 1200 UTC 10 March 2016 (g) 0000 UTC 11 March 2016 (h) 1200 UTC 11 March 2016 (i) 0000 UTC 12 March 2016 (j) 1200 UTC 12 March 2016 . The L indicates the position of the 500 hPa full inversion geopotential height minimum for each time step.

500 hPa Geopotential Height Perturbations (m)					
UTC	Hours After 0000 UTC 08 March	NCEP Final Analysis	TOT_{PERT}	U_{PERT}	L_{PERT}
0000 08 March	0	-244.0876	-242.9593	-253.1447	10.1854
0600	6	-278.8303	-278.0814	-287.5535	9.4721
1200	12	-329.9881	-342.8355	-324.3658	-18.4697
1800	18	-311.2504	-311.0917	-309.8330	-1.2587
0000 09 March	24	-317.0188	-316.2919	-296.8883	-19.4036
0600	30	-322.5992	-322.0874	-294.4583	-27.6291
1200	36	-328.8594	-328.5822	-280.5346	-48.0476
1800	42	-301.7371	-308.8327	-262.4935	-46.3392
0000 10 March	48	-293.026	-301.1916	-239.2405	-61.9511
0600	54	-284.7255	-285.3916	-223.5090	-61.8826
1200	60	-277.7493	-282.4849	-214.9056	-67.5793
1800	66	-247.4629	-248.9736	-176.4314	-72.5422
000011 March	72	-226.8952	-228.9486	-134.2130	-94.7356
0600	78	-192.2562	-194.2069	-105.4314	-88.7755
1200	84	-217.6218	-220.1387	-98.8696	-121.2691
1800	90	-172.973	-175.7712	-61.8180	-113.9532
0000 12 March	96	-158.9751	-161.7025	-39.2902	-122.4123
0600	102	-136.2389	-139.1965	-25.9503	-113.2462
1200	108	-141.8836	-145.1155	-19.8956	-125.2199
1800	114	-89.6217	-92.9374	11.2683	-104.2057

Table 2. 500 hPa geopotential height perturbations (m) associated with the NCEP Final Analyses, and the contribution from TOT_{PERT}, U_{PERT}, and L_{PERT} QGPV anomalies from 0000 UTC 08 March – 1800 UTC 12 March.

d. 500 hPa Geopotential Height Perturbation Analysis

The 500 hPa geopotential height perturbation values from Table 2 are then plotted in the same 6-h intervals in Fig. 20. Again, the TOT_{PERT} and NCEP final analysis geopotential height perturbations are very similar, with a RMSE value of 4.3 m. Interestingly enough, this figure shows that the TOT_{PERT}, U_{PERT}, and NCEP final analysis geopotential height perturbations all seem to decrease in magnitude from 00-12 hours after 0000 UTC 08 March, but then begin to weaken for the remainder of the period. In other words, the 500 hPa geopotential height perturbation decreases in magnitude, confirming that the 500 hPa cyclone underwent slow, but systematic weakening throughout nearly the entire event. The geopotential height perturbations associated with the L_{PERT} QGPV anomaly, however, increase throughout the evolution of the 500 hPa trough, indicating that the lower-level QGPV anomaly actually helped to strengthen the cyclone.

Nevertheless, the lower-level QGPV anomaly still had much less influence on the overall 500 hPa geopotential height perturbation field than the upper-level QGPV anomaly. To elaborate, it is evident that the geopotential height perturbations associated with the U_{PERT} QGPV anomaly contribute most to the geopotential height perturbations associated with the $TOT_{PERT.}$ This indicates that the upper-level QGPV anomaly influenced the 500 hPa geopotential height perturbations more substantially than the lower-level QGPV anomaly. In fact, the geopotential height perturbations associated with the U_{PERT} QGPV anomaly account for 73% of the total geopotential height perturbations over the entire five-day period. To expand, if all the geopotential height perturbations associated with U_{PERT} over the entire time interval were summed together and then divided by the sum of the total geopotential height

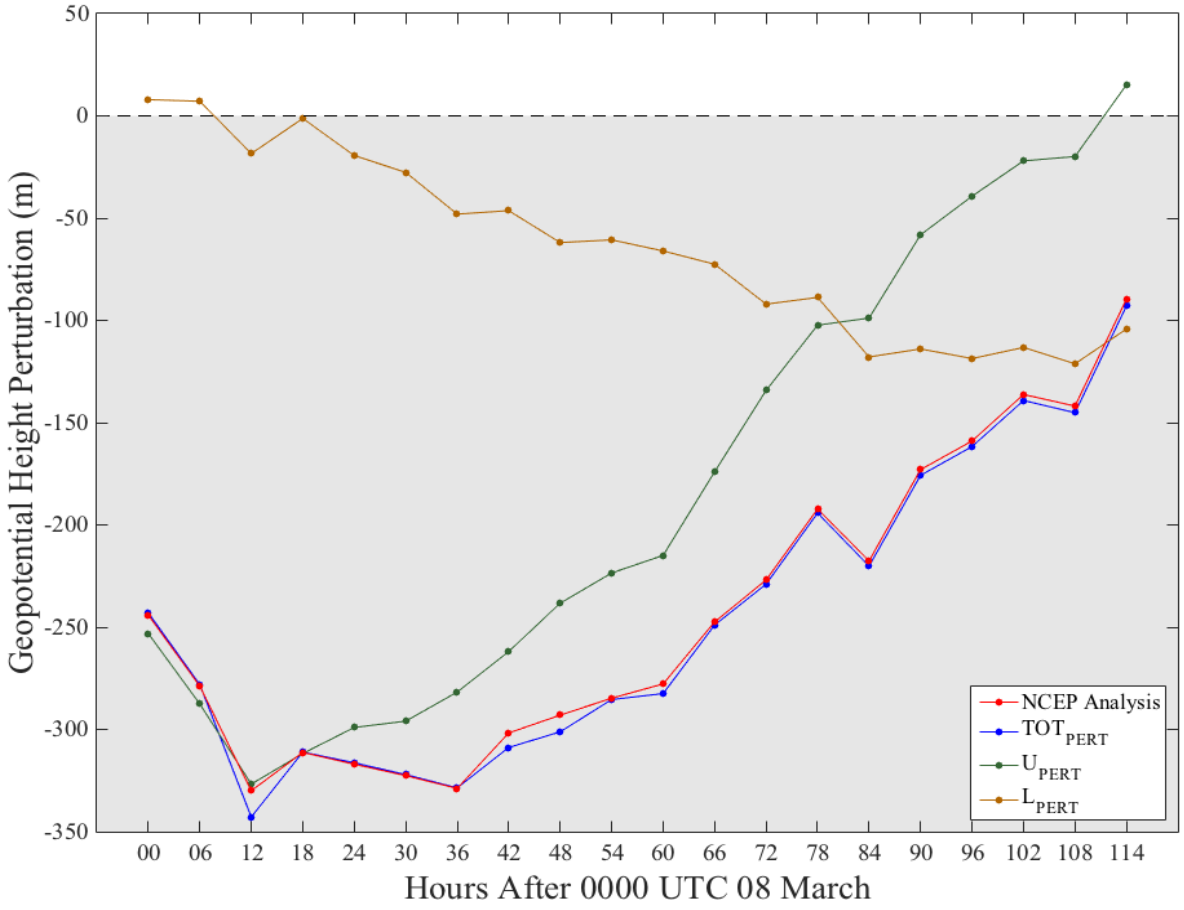

Figure 20. The 6-hour total geopotential height perturbations (TOT_{PERT}) at the location of the fully inverted 500 hPa geopotential height minimum and its two discrete perturbation layers (U_{PERT} and L_{PERT}). The GFS final analysis 500 hPa geopotential height perturbations are also shown.

perturbations associated with TOT_{PERT}, the resulting ratio would result in about 73%. Thus, this analysis suggests that the tropopause-level QGPV anomaly exerted the dominant influence on the 500 hPa geopotential height perturbations associated with this anomalous trough.

e. 500 hPa Geopotential Height Tendency Analysis

To further expand on the previous analysis, this study also evaluated the *tendency* in 500 hPa geopotential height perturbations at the position of the full inversion geopotential height minimum (the location of the L's) between successive 6-h intervals for each of the following fields: NCEP final analysis, TOT_{PERT}, U_{PERT}, and L_{PERT}. Figure 21 presents a summary of the 6-hourly evolution of geopotential height perturbation tendency determined via a forward difference approximation. This figure shows that the geopotential height perturbation tendency associated with the U_{PERT} QGPV anomaly are most significant to the total geopotential height perturbations changes (TOT_{PERT}), as represented by the close relationship of both lines on the figure and a RMSE value of 5.1 m. This figure also illustrates that the lower-level QGPV anomaly had a lesser impact on the 500 hPa geopotential height perturbation tendency over the entire five-day event, as the line is seen nearly oscillating about the 0 m geopotential height tendency line, with a majority of the line staying slightly below the 0 m threshold throughout the entire five days. Thus, it can be stated that on average over the five-day event, the lower-level QGPV anomaly did not have as much of an impact as the upper-level QGPV anomaly on 500 hPa geopotential height perturbation tendency, consistent with the results obtained in Fig. 20 that just analyzed the 500 hPa geopotential height perturbations at the locations of the minimum. It is also

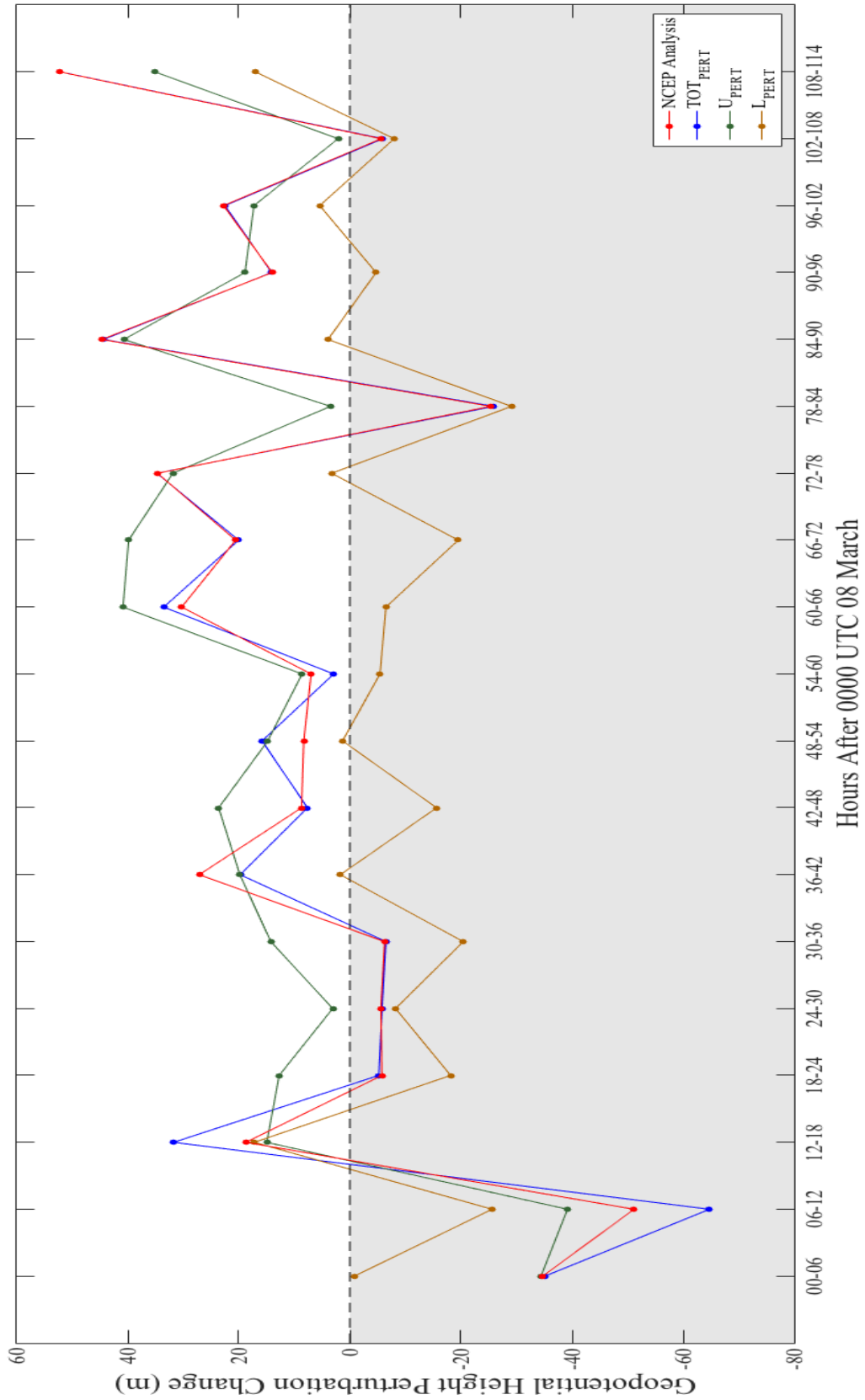

Figure 21. The 6-hourly 500 hPa geopotential height perturbation tendency at the position of the fully inverted 500 hPa geopotential height minimum, computed via a forward difference approximation.

interesting to note that the height tendency analysis on Fig. 21 also points to the fact that generally over the five-day event, the 500 hPa upper-level trough is actually weakening, despite becoming more anomalous throughout its evolution. This supports the idea that it was not necessarily the deepening of the geopotential heights that made the trough anomalous, but rather the southern extent it reached during early-to-mid March that classified it as a 12-sigma event.

3.3. Further analysis of 10 March 2016 including QGPV Inversion

A final goal of this research is to further investigate the forcing mechanisms that may have led to the extreme flooding on 10 March when parts of northern Louisiana received more than 50% of the total rainfall from the entire five-day event (Fig. 22). To accomplish this task, the same static QGPV inversion is utilized to explore the PGMF over this state. Additional analysis into the synoptic and mesoscale features and forcings that may have played a role in producing the high rainfall totals reported on this date is also performed here.

From 0000 UTC 08-10 March, it can be seen that the 850 hPa flow becomes increasingly meridional over Louisiana during this period (Figs. 4c, 5c, and 6c). Associated with this increase in meridional flow is low-level poleward moisture flux convergence. It is important to note that since the poleward geostrophic flow (v_g) adequately approximates the full poleward flow (v) at 850 hPa (~ 5 m s^{-1} difference in the area of interest), the PGMF serves as an adequate representation of the total poleward moisture flux. Therefore, the PGMF will be used in the following analysis. Figure 23a shows this maximum positive PGMF across the southcentral U.S. as part of the GFS final tropospheric analysis data valid

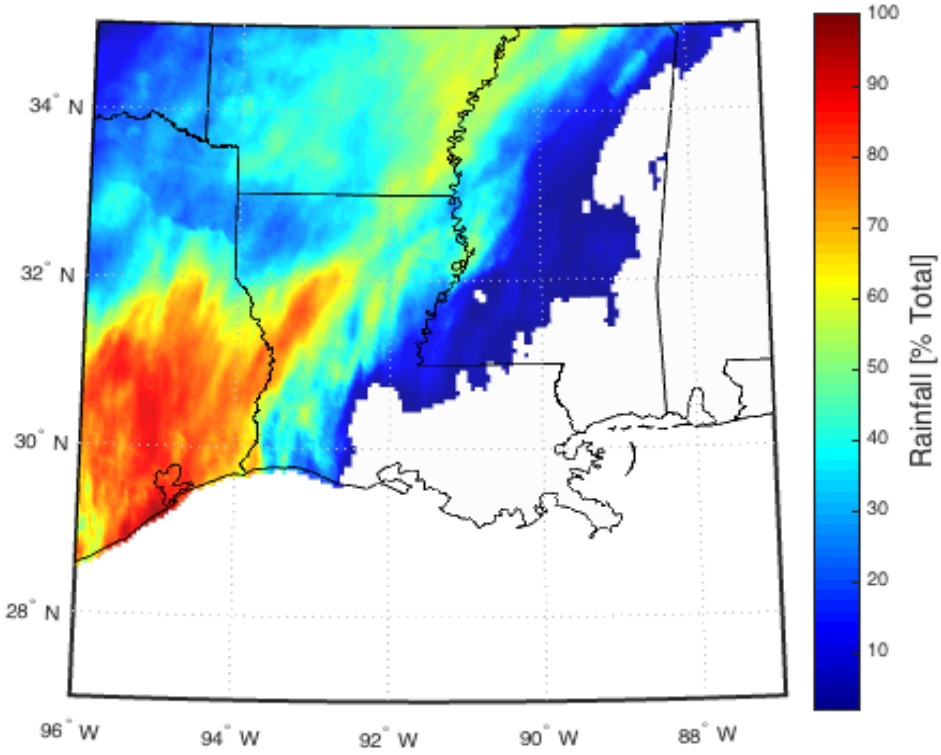

Figure 22. Amount of rainfall total that fell on 10 March 2016 as a percentage of the 5-day total. Data provided by the National Weather Service's Advanced Hydrologic Prediction Service.

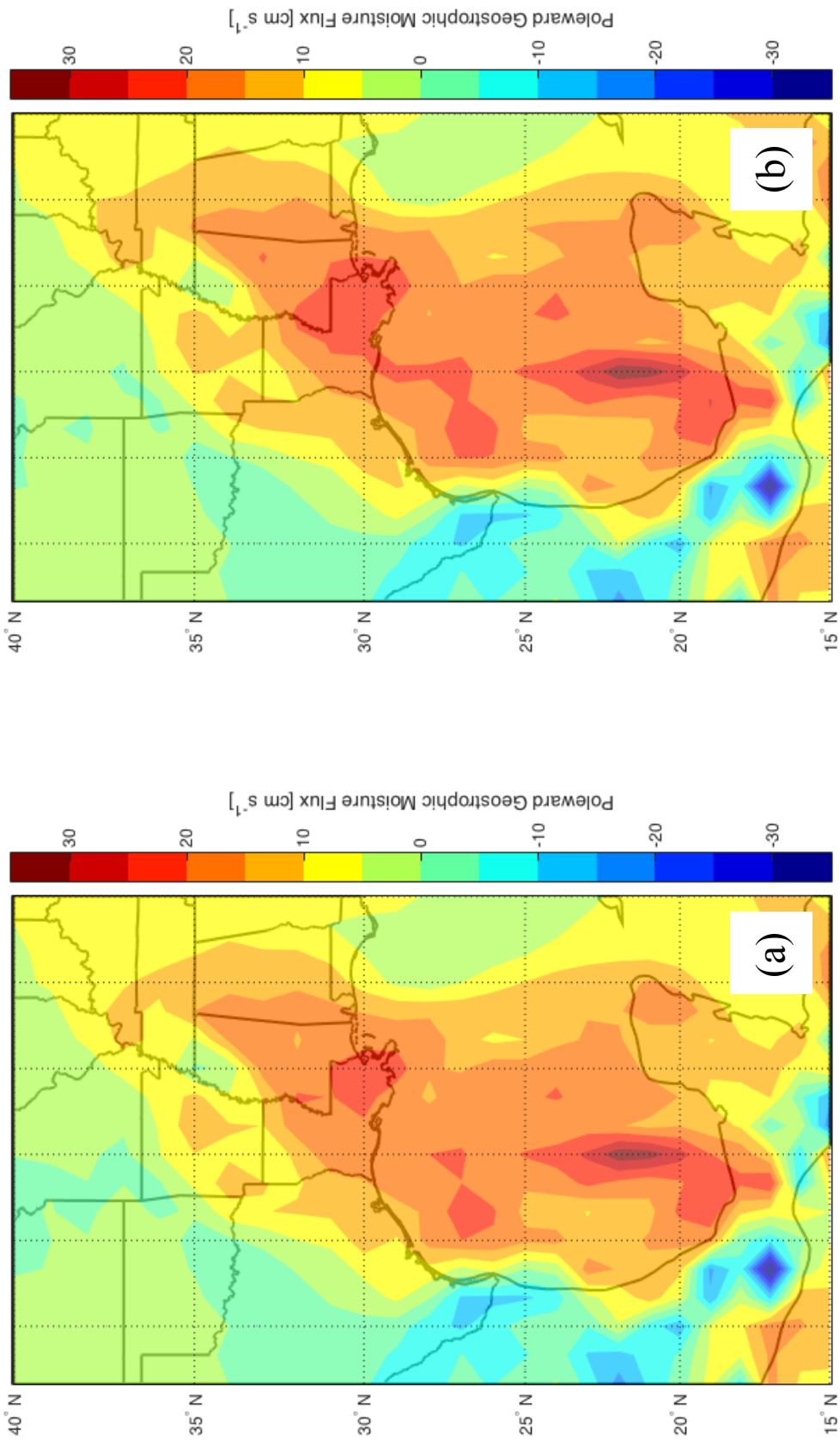

Figure 23. . 0000 UTC 10 March 2016: (a) 850 hPa PGMF associated with the full atmosphere QGPV inversion (b) 850 hPa PGMF associated with the NCEP final analysis

at 0000 UTC 10 March. It can be seen that parts of northern Louisiana experienced PGMF values around 10-15 cm s^{-1}, whereas parts of southeastern Louisiana, including cities such as New Orleans, experienced larger PGMF values on the order of 20-25 cm s^{-1}. The greatest PGMF was located in the Gulf of Mexico along the 93° W longitude border with observed values greater than 30 cm s^{-1}. Overall, it can be seen that large amounts of low-level moisture were advancing into the region presumably associated with the positioning of the upper-level trough. To more quantitatively assess the 850 hPa PGMF, the same static QGPV inversion was utilized. Just as before, similar checks regarding the PGMF had to be completed before using the results of the QGPV inversion. Figure 23b shows the PGMF associated with the full QGPV inversion, similar to that shown of the GFS analysis in Fig. 23a. As shown, both diagrams are similar both in magnitude and distribution of the PGMF, and thus, it can be assumed that any PGMF results obtained from using the full static QGPV inversion technique are reliable. Immediately noticeable on both figures are the negative PGMF values located over southern Texas and central Mexico and the positive PGMF values located over the Gulf of Mexico and into the southcentral U.S. It is important to note that the mixing ratios across this domain were constant for calculations of the PGMF in both the full inversion and analysis. As a result, the resulting PGMF was a direct consequence of a difference in the meridional component of the geostrophic wind (Vg) between the full inversion and analysis. This analysis focuses on the positive PGMF values because they represent northward moisture advection from the Gulf of Mexico into the southcentral U.S., and range from ~10-35 cm s^{-1}, with PGMF magnitudes of ~15-25 cm s^{-1} located specifically over the state of Louisiana.

As done previously, the PGMF associated with the full QGPV inversion was then separated into its respective mean (not shown) and perturbation fields in a process identical to that when evaluating changes in the 500 hPa geopotential height perturbations associated with the upper-level trough. The PGMF associated with the total QGPV anomaly (TOT_{PERT}) is seen in Fig. 24. There is maximum positive PGMF of ~ 30 cm s^{-1} located again on the 93° W longitude line located over the southwestern Gulf of Mexico. In addition, PGMF magnitudes of 5-10 cm s^{-1} can be seen over most of the southcentral U.S. There is also an enhanced area of PGMF located over the central and southern portions of Louisiana and Mississippi, specifically, on the order of 15-20 cm s^{-1}.

To evaluate the impact of upper- and lower- QGPV anomalies on the PGMF at this time, the PGMF associated with the total atmosphere QGPV anomaly (TOT_{PERT}) was further partitioned, as seen in Figs. 25a and 25b. Figure 25a shows PGMF values that were a result of the upper-level QGPV anomaly and range from 5-10 cm s^{-1} over all areas in the domain, with enhanced values of 15-20 cm s^{-1} over far western portions of the Gulf of Mexico, far eastern Texas, and the majority of the state of Louisiana. On the other hand, Fig. 25b shows far smaller magnitudes of PGMF of about 0-5 cm s^{-1} over the majority of the Gulf of Mexico, far southeastern Louisiana, eastern and southern Mississippi, and western Alabama. It is interesting to note that the PGMF associated with the U_{PERT} QGPV anomaly contributed about 60% of the PGMF associated with the total atmosphere QGPV anomaly. Thus, this analysis also indicates, as before, that the circulation associated with the upper-level QGPV anomaly exerted a greater influence, even on the PGMF at 850 hPa, than that associated with the lower-level QGPV anomaly.

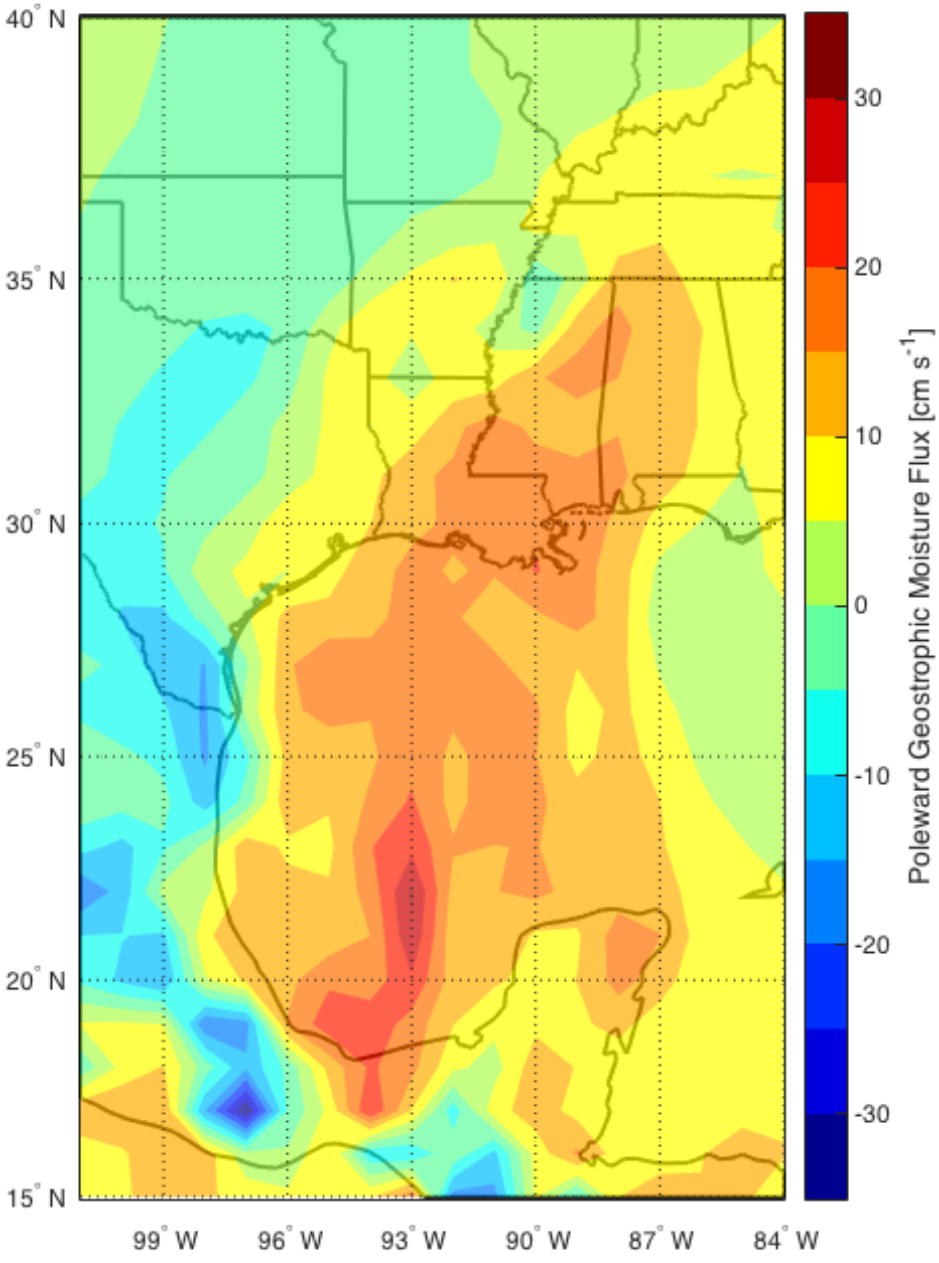

Figure 24. 0000 UTC 10 March: 850 hPa PGMF associated with the TOT_{PERT} QGPV anomaly.

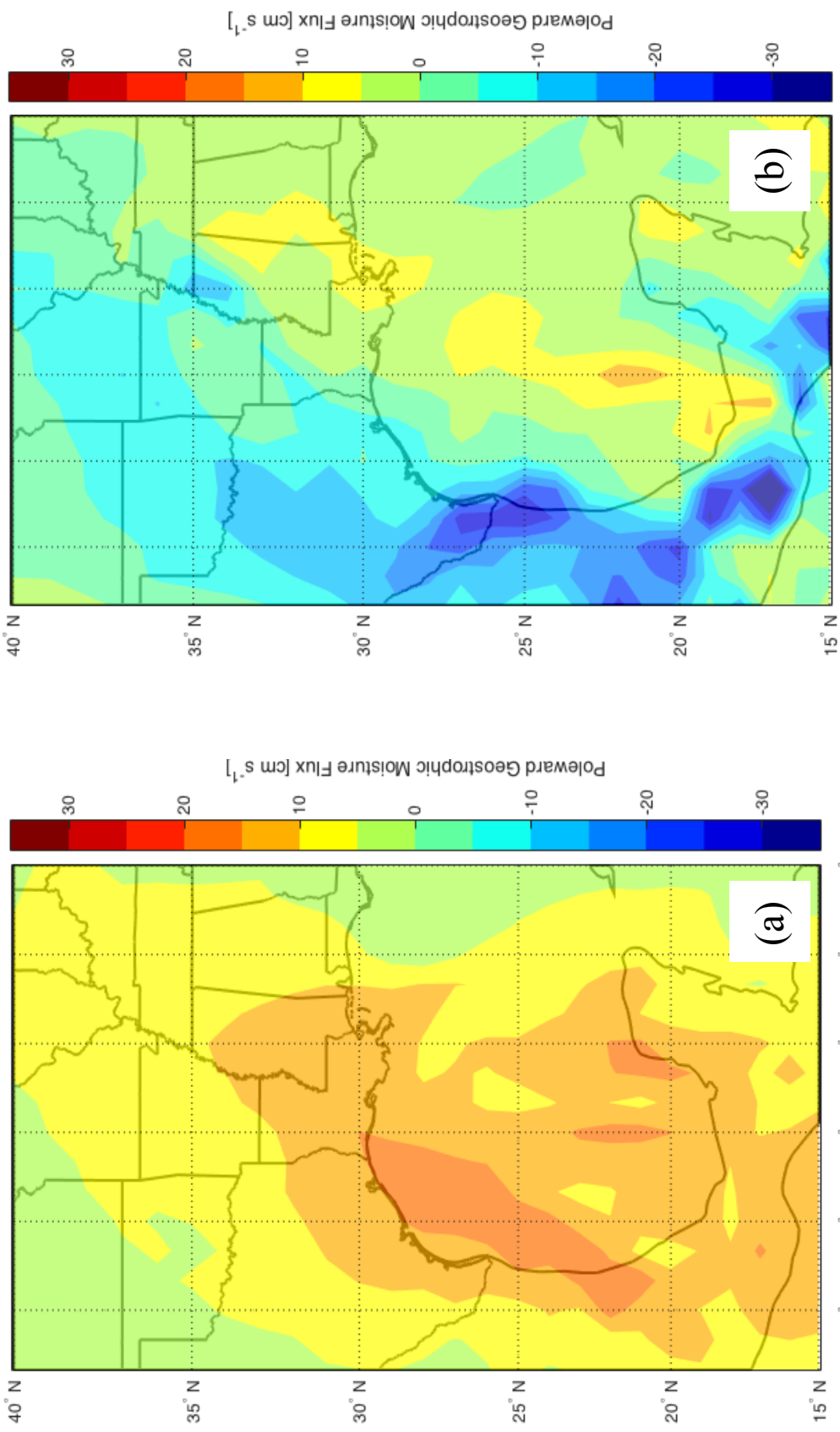

Figure 25. 0000 UTC 10 March: (a) 850 hPa PGMF associated with the U_{PERT} QGPV anomaly and (b) PGMF associated with the L_{PERT} QGPV anomaly.

In addition to the PGMF located over the southcentral U.S. at this time, there were other mesoscale influences that helped contribute to the record-breaking rainfall on this date. Due to the linear nature of the convection that formed (Fig. 7), low-level (850 hPa) frontogenesis was investigated. Figure 26 depicts the 850 hPa horizontal frontogenesis at 0600 UTC 10 March, with values ranging from 4-8 K $(1000\ km)^{-1}$ $(3\ hours)^{-1}$ occurring over a linear boundary that extends from southeast Texas through the central and northern portions of Louisiana and into parts of Mississippi, Arkansas, and Tennessee. Also depicted in Fig. 26 is the 850 hPa negative omega field (ω), showing that the frontogenesis forcing corresponded to rising motion. To more effectively analyze the ω distribution, a cross-section was taken across this region of horizontal frontogenesis and the results are seen in Fig. 27. This cross-section shows horizontal frontogenesis occurring in a deep layer of the troposphere, with largest magnitudes located in the layer of 400 hPa to near the surface. Potential temperatures and the negative ω field are also shown on this cross-section, with a large amount of rising motion located to the warm side of the region of frontogenesis, with a maximum of $\sim 20 \times 10^{-3}$ Pa s^{-1} at about the 500 hPa level. Horizontal frontogenesis promotes a thermally direct circulation that forces warm air to rise and cool by expansion. This forced ascent is clearly evident in the cross-section. As then might be expected, convection became focused along this south-southwest to north-northeast-oriented boundary, as supported by the radar image seen previously in Fig. 7.

A sounding for Slidell, LA taken at 0000 UTC 10 March (Fig. 28) is characterized by low-level moisture and saturation from the surface to about 800 hPa surmounted by warm and dry air within the 700 - 400 hPa layer. This sounding profile is most likely due to the

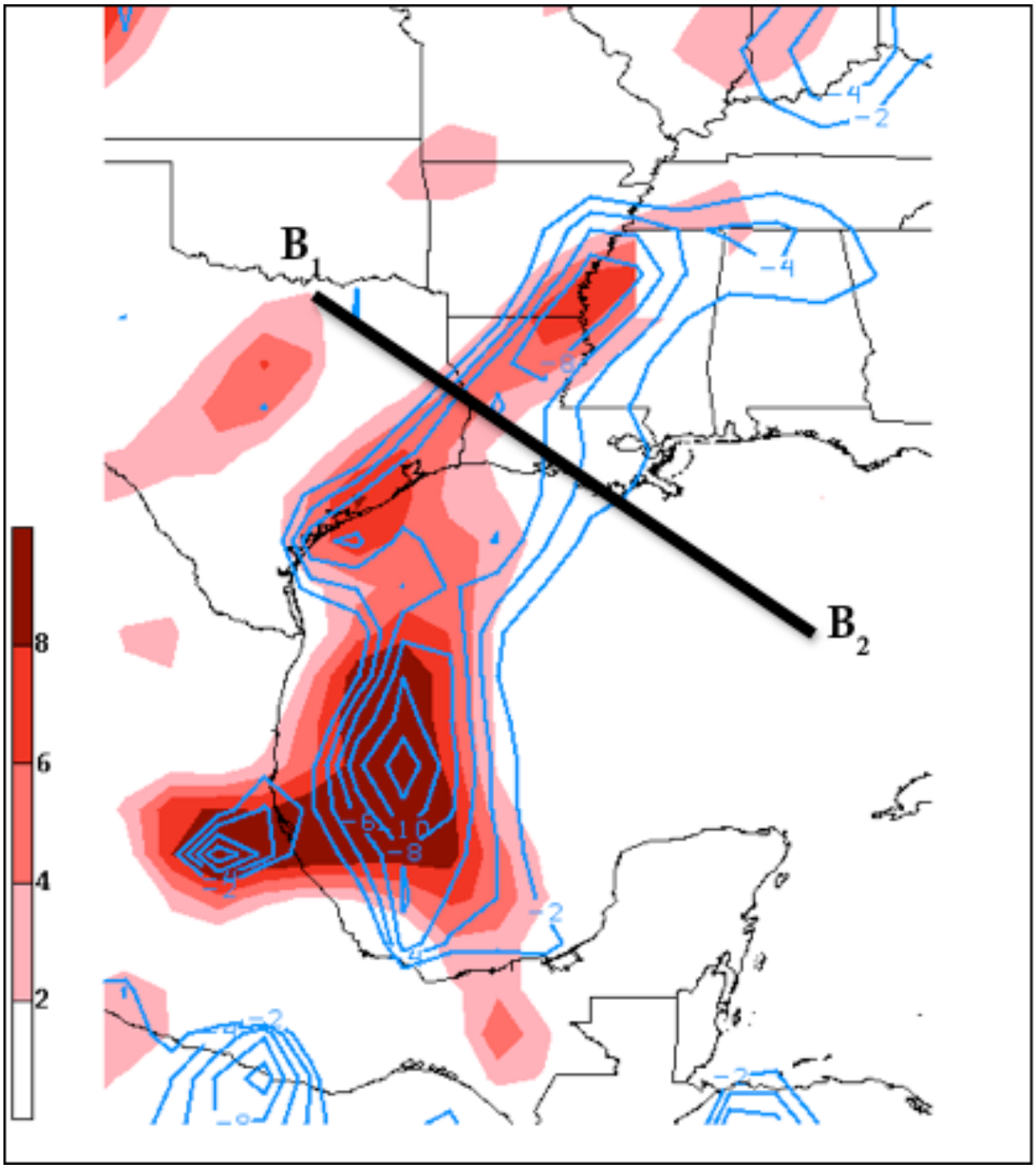

Figure 26. 0600 UTC 10 March 2016 850 hPa horizontal frontogenesis (shaded) in units of every 2 K (1000 km)$^{-1}$ (3 hours)$^{-1}$ and omega (contoured) every 2x10^{-3} Pa s^{-1} with a cross-section along B_1 to B_2.

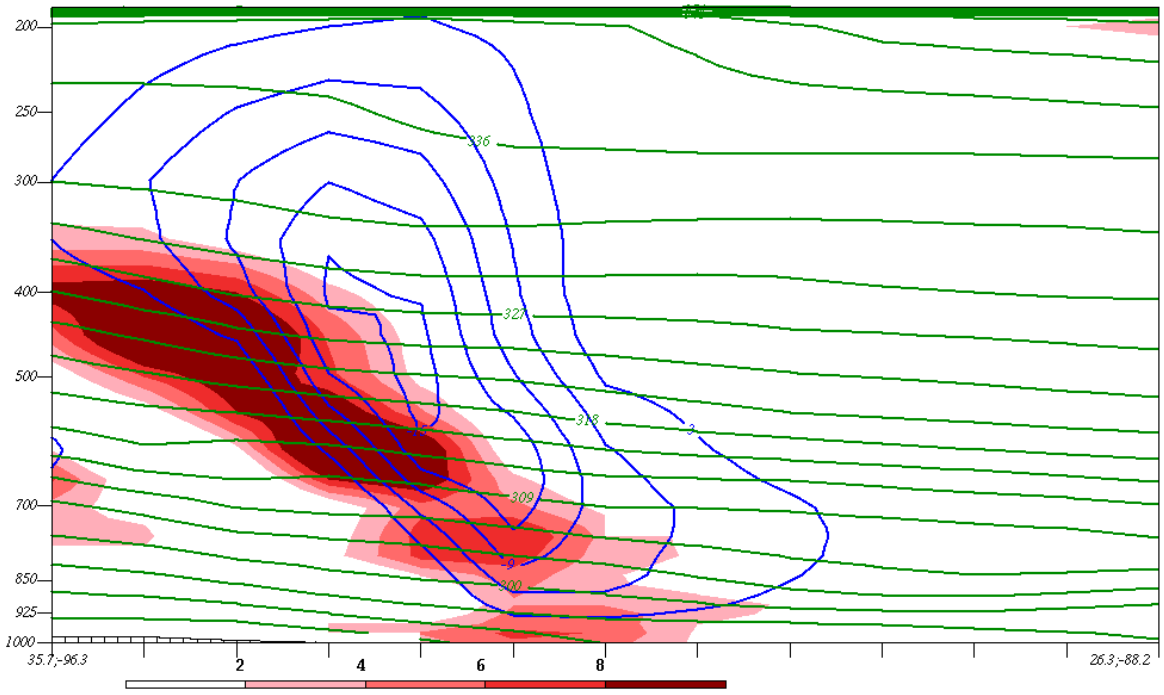

Figure 27. Cross-section from B_1 to B_2 in Figure 26. Horizontal frontogenesis (red fill) in units of every 2 K (1000 km)$^{-1}$ (3 hours)$^{-1}$, omega (blue contoured) every 3 kPa s^{-1}, and potential temperature (green contour) every 3 K.

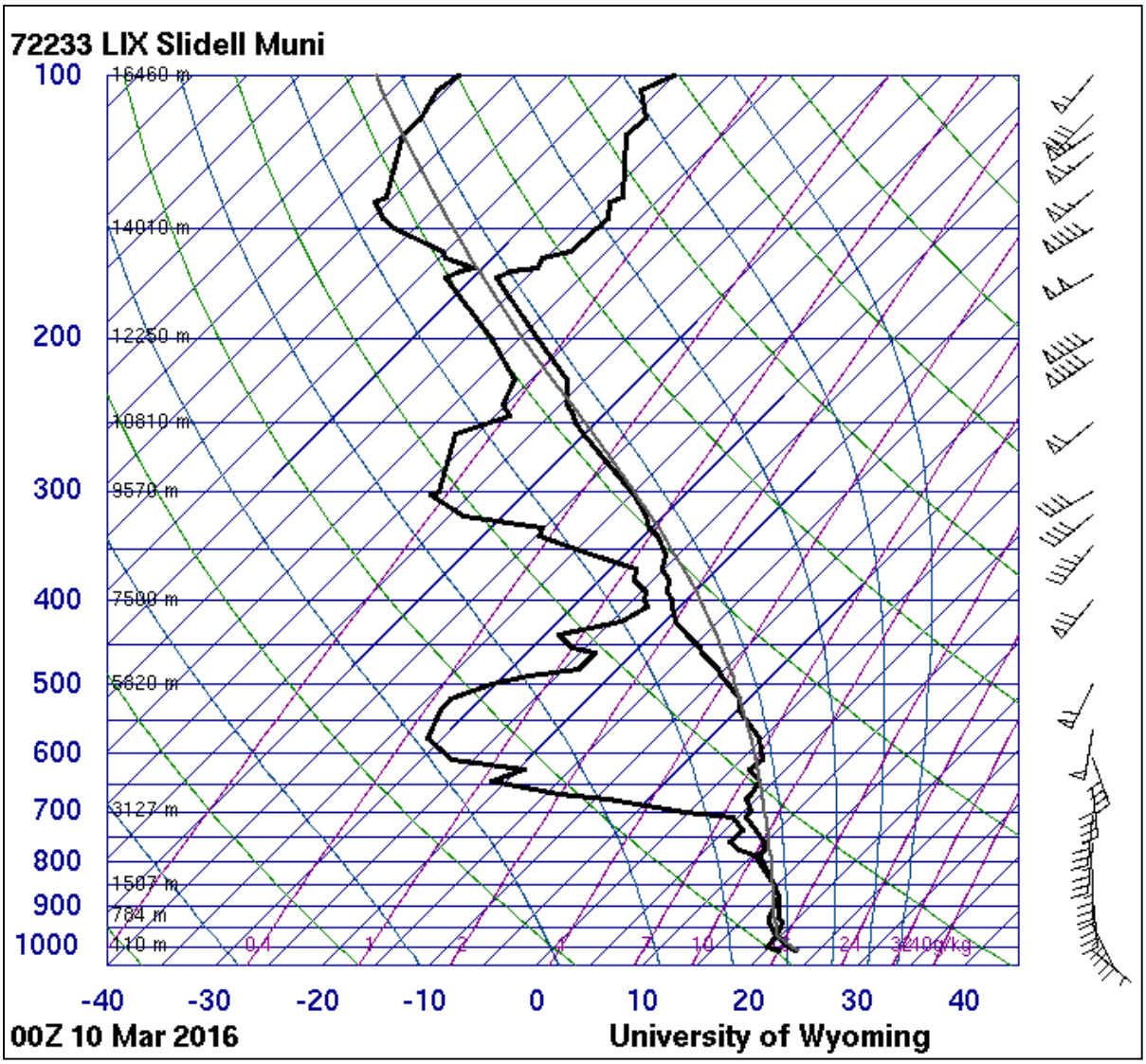

Figure 28. 0000 UTC 10 March 2016 atmospheric sounding profile of Slidell Muni, LA. Data provided by the University of Wyoming.

position of the upper-level trough at this time, as it advected dry middle-to-upper tropospheric air from the Mexican plateau over the Gulf of Mexico, while the lower-levels were saturated. This specific type of vertical sounding illustrates an environment that is strongly convectively unstable in the middle troposphere (i.e. from 800-600 hPa) while also characterized by a surface CAPE value of 360 J kg^{-1} and a lifted index of -0.75. Together, these environmental parameters indicate an atmosphere conducive to the development of locally heavy precipitation and thunderstorms.

The combination of PGMF driven mostly by the upper-level QGPV anomaly, a convectively unstable atmosphere (itself driven primarily by the circulation associated with the upper-level QGPV anomaly), and modest frontogenetic forcing helps explain why parts of northern Louisiana received such extraordinary rainfall on this day.

3.4. Discussion

As in every investigation, it is important to address some of the caveats associated with the analysis technique, in this case, the static QGPV inversion. The effects of diabatic, frictional, topographic, and nonquasigeostrophic processes were neglected when performing the static QGPV inversion. The lack of topographic information (especially over Mexico) may have had an impact on the overall analysis of the 850 hPa PGMF, yet the close PGMF distribution associated with the NCEP final analysis and the full QGPV inversion helped establish the credibility of results of the inversion. The 500 hPa geopotential height tendency analysis completed in this study is also at a level at which these processes can be assumed to be negligible. This study also uses a bookend mean and perturbation scheme to

assess the 500 hPa geopotential height perturbations and 850 hPa PGMF when conducting the QGPV inversion. As previously mentioned, there exists no definitive time mean and it can be calculated in any way, but this choice can greatly impact the overall results of the inversion. Accordingly, it is important to address the fact that other methods of choosing a mean may also provide alternative, but reliable results.

4. CONCLUSION

This case study presented a multi-scale dynamical analysis of the anomalous upper-level trough that propagated over central and southern Mexico from 08-12 March 2016 and caused a major flooding event for portions of the southcentral U.S. The first half of this research focused on the development and influence of an upper-level front on the southeastward propagation of the upper-level trough. To examine this front further, a Sawyer–Eliassen circulation diagnostic was utilized. It was found that in the region of geostrophic cold air advection in cyclonic shear off of the coast of California on 0000 UTC 08 March, an upper-level front had developed in response to subsidence induced along the jet core. This subsidence acted to subduct higher PV from the lower stratosphere into the middle and upper troposphere. While in northwesterly flow, this PV was then advected horizontally to the southeast where the associated geopotential heights falls at successively southern latitudes directly contributing to the anomalous southern latitude eventually reached by this trough.

To further quantify the synoptic evolution of the upper-level trough, a static QGPV inversion developed by Hakim et al. (1996) and later used by Nielsen-Gammon and Lefevre (1996) was performed. Using a methodology very similar to that employed by Martin and

Marsili (2002) with Ertel PV inversion, the results of the QGPV inversion showed that the 500 hPa geopotential height perturbations were most influenced by the QGPV anomaly at the upper-troposphere, accounting for nearly 73% of the total geopotential height perturbations associated with the total QGPV anomaly. Thus, the preceding analysis and results suggests that the evolution of the trough was primarily governed by the QGPV anomaly situated in the upper troposphere, in coordination with the development and influence of an upper-level front.

The static QGPV inversion process was also used to gain additional insight into the 850 hPa PGMF over the southcentral U.S. on 0000 UTC 10 March 2010. These results also showed the dominant influence of the upper-level QGPV anomaly as its circulation accounted for nearly 60% of the PGMF that contributed to the heavy rain on 10 March. Earlier investigation into this date also showed 850 hPa frontogenesis and associated forcing for ascent located over Louisiana in an environment that was also characterized by convective instability. These factors, combined with enhanced PGMF flux convergence driven primarily by an upper-tropospheric QGPV anomaly, all collaborated to produce an environment conducive to the production of record-breaking rainfall and locally severe convection.

The above conclusions help to provide insight into the upper-level trough that characterized this March 2016 extreme flooding event. This research also helped present a better understanding of some of the factors that were involved in causing the extensive flooding that may lay the groundwork for future studies of this case.

5. FUTURE WORK

In light of these results, several science issues present themselves as opportunities for expanded thought and additional work. First, future research may continue to utilize the static QGPV inversion to evaluate geopotential height tendencies, but rather than evaluating the geopotential height perturbations at the location of the geopotential height minima (the L's), one might consider, for example, a 3° x 3° box centered about the grid point with the lowest recorded geopotential height to develop a nine-point average of the minimum geopotential height to use in the diagnostics. This method may then help reduce the noise associated with the analysis. Another way to improve upon this research would be to evaluate geopotential height changes at a pressure level that is mid-way between the defined upper- and lower-layers. This study analyzed both the 500 hPa geopotential height perturbations and their 6-h tendencies. Since the upper-layer was defined as including the 500-50 hPa levels, by definition, the 500 hPa level is encompassed within the upper-layer. Logically, one may then infer that the results would favor the upper-level QGPV anomaly as having a greater impact on the geopotential height perturbations at this level due to the fact this level is incorporated within the defined upper-layer. By choosing a level mid-way between the defined upper-and lower layers, it can be reasoned that both the upper-level and lower-level QGPV anomalies have equal chances of influencing the geopotential height perturbations at that newly set level.

Further investigation into the close proximity, or superposition, of the polar and subtropical jets should be considered when analyzing the magnitude of the ageostrophic subsidence associated with these jets for this particular case. Other studies (i.e. Winters and

Martin 2014) investigated the impact of jet superposition on the ageostrophic circulations associated with upper-level fronts, and found that the superposition can enhance the subsidence associated with upper-level fronts. Thus, enhanced amounts of PV from the lower stratosphere could be subducted into the middle- and upper-troposphere, and if in northwesterly flow, could be advected to the southeast and promote further deepening of the upper-level trough. It would be of great interest to investigate the possibility of such a superposition event during the March 2016 case.

Finally, it would be insightful to use these similar diagnostics and procedures to study other high impact weather events that are characterized by anomalous upper-level troughs in northwesterly flow. More specifically, a study could be conducted that first identified similar low-latitude troughs in late winter/early spring and then performed the QGPV analysis of their associated rainfall in the U.S. More complete investigations and comparisons between the March 2016 event and others may provide insightful results that could aid in the forecasting of severe flooding events over the southcentral U.S.

REFERENCES

Charney, J. G., and M. E. Stern, 1962: On the Stability of Internal Baroclinic Jets in a Rotating Atmosphere. *J. Atmos. Sci.*, **19**, 159–172, doi:10.1175/1520-0469(1962)019<0159:OTSOIB>2.0.CO;2.

Danielsen, E. F., 1964: *PROJECT SPRINGFIELD REPORT*. ISOTOPES INC WESTWOOD NJ, ISOTOPES INC WESTWOOD NJ, http://www.dtic.mil/docs/citations/AD0607980 (Accessed July 19, 2017).

Davis, C. A., and K. A. Emanuel, 1991: Potential Vorticity Diagnostics of Cyclogenesis. *Mon. Wea. Rev.*, **119**, 1929–1953, doi:10.1175/1520-0493(1991)119<1929:PVDOC>2.0.CO;2.

Kleinschmidt, E., 1957: Cyclones and anticyclones. *Dynamic Meteorology*. *Handbuch det Physik,* **49**, S. Flugge, Ed., Springer-Verlag, 112-154

Eliassen, A., 1962: On the Vertical Circulation in Frontal Zones. *Geofys*. *Publ*., **24**, 147-160

Emanuel, K., M. Fantini, and A. Thorpe, 1987: Baroclinic Instability in an Environment of Small Stability to Slantwise Moist Convection. Part I: Two-Dimensional Models: Journal of the Atmospheric Sciences: Vol 44, No 12. http://journals.ametsoc.org/doi/abs/10.1175/1520-0469(1987)044%3C1559:BIIAEO%3E2.0.CO%3B2 (Accessed July 19, 2017).

Hakim, G. J., D. Keyser, and L. F. Bosart, 1996: The Ohio Valley Wave-Merger Cyclogenesis Event of 25–26 January 1978. Part II: Diagnosis Using Quasigeostrophic Potential Vorticity Inversion. *Mon. Wea. Rev.*, **124**, 2176–2205, doi:10.1175/1520-0493(1996)124<2176:TOVWMC>2.0.CO;2.

Hoskins, B. J., M. E. McIntyre, and A. W. Robertson, 1985: On the use and significance of isentropic potential vorticity maps. *Q.J.R. Meteorol. Soc.*, **111**, 877–946, doi:10.1002/qj.49711147002.

Keyser, D., and M. J. Pecnick, 1985: A Two-Dimensional Primitive Equation Model of Frontogenesis Forced by Confluence and Horizontal Shear. *J. Atmos. Sci.*, **42**, 1259–1282, doi:10.1175/1520-0469(1985)042<1259:ATDPEM>2.0.CO;2.

——, and M. A. Shapiro, 1986: A Review of the Structure and Dynamics of Upper-Level Frontal Zones. *Mon. Wea. Rev.*, **114**, 452–499, doi:10.1175/1520-0493(1986)114<0452:AROTSA>2.0.CO;2.

——, M. J. Pecnick, and M. A. Shapiro, 1986: Diagnosis of the Role of Vertical Deformation in a Two-Dimensional Primitive Equation Model of Upper-Level Frontogenesis. *J. Atmos. Sci.*, **43**, 839–850, doi:10.1175/1520-0469(1986)043<0839:DOTROV>2.0.CO;2.

Korner, S. O., and J. E. Martin, 2000: Piecewise Frontogenesis from a Potential Vorticity Perspective: Methodology and a Case Study. *Mon. Wea. Rev.*, **128**, 1266–1288, doi:10.1175/1520-0493(2000)128<1266:PFFAPV>2.0.CO;2.

Lackmann, G. M., and J. Gyakum, Heavy Cold-Season Precipitation in the Northwestern United States: Synoptic Climatology and an Analysis of the Flood of 17–18 January 1999: Weather and Forecasting: Vol 14, No 5. http://journals.ametsoc.org/doi/abs/10.1175/1520-0434(1999)014%3C0687:HCSPIT%3E2.0.CO%3B2 (Accessed July 19, 2017).

——, D. Keyser, and L. F. Bosart, 1997: A Characteristic Life Cycle of Upper-Tropospheric Cyclogenetic Precursors during the Experiment on Rapidly Intensifying Cyclones over the Atlantic (ERICA). *Mon. Wea. Rev.*, **125**, 2729–2758, doi:10.1175/1520-0493(1997)125<2729:ACLCOU>2.0.CO;2.

Lang, A. A., and J. E. Martin, 2012: The structure and evolution of lower stratospheric frontal zones. Part 1: Examples in northwesterly and southwesterly flow. *Q.J.R. Meteorol. Soc.*, **138**, 1350–1365, doi:10.1002/qj.843.

Otkin, J. A., and J. E. Martin, 2004. A synoptic-climatology of the subtropical Kona storm. *Mon. Wea. Rev.*, **132**, 1502-1517

Martin, J., 2006: Wiley: Mid-Latitude Atmospheric Dynamics: A First Course - Jonathan E. Martin. http://www.wiley.com/WileyCDA/WileyTitle/productCd-0470864656.html (Accessed July 19, 2017).

Martin, J. E., 2014: Quasi-geostrophic diagnosis of the influence of vorticity advection on the development of upper level jet-front systems. *Q.J.R. Meteorol. Soc.*, **140**, 2658–2671, doi:10.1002/qj.2333.

——, and N. Marsili, 2002: Surface Cyclolysis in the North Pacific Ocean. Part II: Piecewise Potential Vorticity Diagnosis of a Rapid Cyclolysis Event. *Mon. Wea. Rev.*, **130**, 1264–1281, doi:10.1175/1520-0493(2002)130<1264:SCITNP>2.0.CO;2.

Mudrick, S. E., 1974: A Numerical Study of Frontogenesis. *J. Atmos. Sci.*, **31**, 869–892, doi:10.1175/1520-0469(1974)031<0869:ANSOF>2.0.CO;2.

National Centers for Environmental Prediction/National Weather Service/NOAA/U.S. Department of Commerce, 2000: NCEP FNL Operational Model Global Tropospheric Analyses, continuing from July 1999. Research Data Archive at the National Center for Atmospheric Research, Computational and Information Systems Laboratory, Boulder, CO. [Available online at https://doi.org/10.5065/D6M043C6.] Accessed 05 21 2017.

Nielsen-Gammon, J. W., and R. J. Lefevre, 1996: Piecewise Tendency Diagnosis of Dynamical Processes Governing the Development of an Upper-Tropospheric Mobile Trough. *J. Atmos. Sci.*, **53**, 3120–3142, doi:10.1175/1520-0469(1996)053<3120:PTDODP>2.0.CO;2.

NOAA - National Weather Service - Water. https://water.weather.gov/ahps/ (Accessed July 31, 2017).

NOAA's NWS Storm Prediction Center. http://www.spc.noaa.gov/archive/ (Accessed July 31, 2017).

NWS Flood Safety Home Page. http://www.floodsafety.noaa.gov/ (Accessed July 31, 2017).

Over 26 Inches of Rain Triggers Record Flooding in the South, Including the Sabine River. *The Weather Channel*,. https://weather.com/storms/severe/news/historic-south-flooding-march-2016?_escaped_fragment_ (Accessed May 19, 2017e).

Posselt, D. J., and J. E. Martin, 2004. The effect of latent heat release on the evolution of a warm occluded thermal structure. *Mon. Wea. Rev.*, **132**, 578-599

Reed, R. J., 1955: A study of a characteristic tpye of upper-level frontogenesis. *J. Meteor.*, **12**, 226–237, doi:10.1175/1520-0469(1955)012<0226:ASOACT>2.0.CO;2.

——, and F. Sanders, 1953: An investigation of the development of a mid-tropospheric frontal zone and its associated vorticity field. *J. Meteor.*, **10**, 338–349, doi:10.1175/1520-0469(1953)010<0338:AIOTDO>2.0.CO;2.

——, and E. F. Danielsen, 1959: Fronts in the vicinity of the tropopause. *Arch. Met. Geoph. Biokl. A.*, **11**, 1–17, doi:10.1007/BF02247637.

Saha, S., and Coauthors, 2010: The NCEP Climate Forecast System Reanalysis. *Bull. Amer. Meteor. Soc.*, **91**, 1015–1057, doi:10.1175/2010BAMS3001.1.

Sanders, F., L. F. Bosart, and C.-C. Lai, 1990: Initiation and Evolution of an Intense Upper-Level Front. *Mon. Wea. Rev.*, **119**, 1337–1367, doi:10.1175/1520-0493(1991)119<1337:IAEOAI>2.0.CO;2.

Sawyer, J. S., 1956: The Vertical Circulation at Meteorological Fronts and Its Relation to Frontogenesis. *Proceedings of the Royal Society of London A: Mathematical, Physical and Engineering Sciences*, **234**, 346–362, doi:10.1098/rspa.1956.0039.

Schultz, D. M., and C. A. Doswell, 1999: Conceptual models of upper-level frontogenesis in south-westerly and north-westerly flow. *Q.J.R. Meteorol. Soc.*, **125**, 2535–2562, doi:10.1002/qj.49712555910.

——, and F. Sanders, 2002: Upper-Level Frontogenesis Associated with the Birth of Mobile Troughs in Northwesterly Flow. *Mon. Wea. Rev.*, **130**, 2593–2610, doi:10.1175/1520-0493(2002)130<2593:ULFAWT>2.0.CO;2.

Shapiro, M., 1981: Frontogenesis and Geostrophically Forced Secondary Circulations in the Vicinity of Jet Stream-Frontal Zone Systems: Journal of the Atmospheric Sciences: Vol 38, No 5. http://journals.ametsoc.org/doi/abs/10.1175/1520-0469(1981)038%3C0954%3AFAGFSC%3E2.0.CO%3B2 (Accessed July 19, 2017).

Shapiro, M. A., 1980: Turbulent Mixing within Tropopause Folds as a Mechanism for the Exchange of Chemical Constituents between the Stratosphere and Troposphere. *J. Atmos. Sci.*, **37**, 994–1004, doi:10.1175/1520-0469(1980)037<0994:TMWTFA>2.0.CO;2.

Stohl, A., and Coauthors, 2003: Stratosphere-troposphere exchange: A review, and what we have learned from STACCATO. *J. Geophys. Res.*, **108**, 8516, doi:10.1029/2002JD002490.

Todsen, M., 1964: *A COMPUTATION OF THE VERTICAL CIRCULATION IN A FRONTAL ZONE FROM THE QUASI-GEOSTROPHIC EQUATIONS.* OSLO UNIV (NORWAY), OSLO UNIV (NORWAY), http://www.dtic.mil/docs/citations/AD0600368 (Accessed July 19, 2017).

University of Wyoming, Atmospheric Soundings. http://weather.uwyo.edu/upperair/sounding.html (Accessed July 31, 2017).

Whitaker, J. S., L. W. Uccellini, and K. F. Brill, 1988: A Model-Based Diagnostic Study of the Rapid Development Phase of the Presidents's Day Cyclone. *Mon. Wea. Rev.*, **116**, 2337–2365, doi:10.1175/1520-0493(1988)116<2337:AMBDSO>2.0.CO;2.

Winters, A. C., and J. E. Martin, 2014: The Role of a Polar/Subtropical Jet Superposition in the May 2010 Nashville Flood. *Wea. Forecasting*, **29**, 954–974, doi:10.1175/WAF-D-13-00124.1.

Storm Events Database | National Centers for Environmental Information. https://www.ncdc.noaa.gov/stormevents/ (Accessed July 19, 2017g).

3 Dead, Thousands Evacuated as Historic Flooding Swamps Louisiana | The Weather Channel. https://weather.com/storms/severe/news/south-severe-weather-flooding-impacts (Accessed July 25, 2017).